

Chapter 4

Structural Engineering of Porous Anodic Aluminum Oxide (AAO) and Applications

Woo Lee

Abstract Porous anodic aluminum oxide (AAO) films can be conveniently produced by anodization of aluminum. Porous oxide layer formed on aluminum contains a large number of mutually parallel pores. Each cylindrical nanopore and its surrounding oxide constitute a hexagonal cell aligned normal to the metal surface. Under proper conditions, the oxide cells are self-organized to form a hexagonally close-packed structure. The novel and tunable structural features of porous AAOs have been intensively exploited for templated synthesis of a variety of functional nanostructures and also for fabrication of nanodevices. On the other hand, porous AAOs with modulated pores may provide an additional degree of freedom in templated synthesis. In addition, they can be used as model systems for systematically investigating structure-property relations of nanostructured materials. Based on the anodization techniques developed recently, one can fabricate porous AAOs with tailor-made internal pore structures. This chapter is devoted to conveying the most recent advances in structural engineering of porous AAOs and nanotechnology applications. In order to provide context, a brief description is given of the general structure and fundamental electrochemical processes associated with pore formation. Subsequently, two common anodizing techniques (i.e., mild and hard anodizations) that have been explored for nanotechnology applications are discussed. Next, various nanostructuring approaches for custom-designed porous AAOs are reviewed. The chapter covers the properties of porous AAOs derived from structural engineering and their applications to various nanotechnology researches and finally presents the challenges and future prospects.

W. Lee (✉)

Department of Physics, Hankuk University of Foreign Studies (HUFS),
Yongin, Daejeon 449-791, Korea
e-mail: woolee@hufs.ac.kr

4.1 Introduction

Anodization of aluminum is an electrochemical oxidation process employed for the formation of protective and decorative coating on aluminum surfaces. In general, the anodic aluminum oxide (AAO) films form with two different morphologies depending on the anodizing electrolytes and conditions; (i) compact nonporous barrier-type AAO films from neutral electrolytes in which the anodic oxide is practically insoluble and (ii) porous-type AAO films from acid electrolytes in which the anodic oxide is slightly soluble [1]. Since the early 1920's, AAO films on aluminum, especially porous AAO films, have received substantial attention in industry due to their diverse applications in electrical insulation, corrosion protection, decoration, and improvement of mechanical properties of aluminum products (e.g., machine parts, architectural items, vehicles, electronic gadgets, outdoor products, etc) [2]. With the discovery of self-organized formation of ordered pore in 1995 [3], the porous-type anodizing processes have been drawing increasing attention in nanotechnology research.

Porous AAO formed on aluminum contains a large number of mutually parallel pores. Each cylindrical pore and its surrounding oxide constitute a hexagonal cell aligned normal to the aluminum surface. Under properly chosen conditions, the oxide cells are self-organized to form a hexagonally close-packed structure, like a honeycomb. Self-ordered porous AAOs with uniform pore diameter in the range of 10–400 nm and with pore density in the range of 10^8 – 10^{10} pores cm^{-2} can be conveniently prepared by simply subjecting aluminum under anodic polarization [4]. The unique and tunable structural features, combined with their excellent thermal stability, chemical inertness, and bio-compatibility, and easy modification of surface chemistry, make porous AAOs not only as ideal templates for synthesizing a variety of functional nanostructures (e.g., nanodots, nanowires, and nanotubes), but also as excellent platform materials for exploring various advanced devices for molecule separation, cell adhesion and culture, drug delivery, chemical/biological sensing, high performance catalyst, information storage, energy storage and harvest, etc. [4–9]. Moreover, based on the recent advances, the pore structure of AAO can be designed and engineered to a variety of geometries (e.g., sharp featured non-circular pores, symmetrically or asymmetrically modulated pores, funnel-like pores, hierarchical three-dimensional architectures of pores, etc.) [4]. The structural engineering of porous AAO can result in the generation of optically active structures by imparting a range of tailored optical properties, such as selective light transmission, reflection, enhancement, confinement, or guide. Therefore, the capability of structural engineering, coupled with the aforementioned characteristics, would make porous AAOs even more versatile as template or platform materials for advanced applications. In fact, utilization of structurally engineered porous AAOs for label-free, real-time, ultra-sensitive chemical and biosensing applications has become an emerging research field during the last few years [10–13].

This chapter conveys the most recent advances in structural engineering of porous AAOs and nanotechnology applications of the resulting porous AAOs. In order to provide context, first a brief description will be given of the general structure and fundamental electrochemical processes associated with pore formation. Subsequently, two common anodizing techniques (i.e., mild anodization (MA) and hard anodizations (HA)) that have been explored for nanotechnology applications will be discussed. Next, various nanostructuring approaches for the fabrication of custom-designed porous AAO architectures will be reviewed. These include micromachining of porous AAO, anodization of pre-textured aluminum, multistep anodization with controlled wet-chemical oxide etching after each anodizing step, programmed potential reduction, pulse anodization (PA) and cyclic anodization (CA) that selectively combine MA and HA processing conditions. The properties of porous AAOs derived from structural engineering and their applications to various nanotechnology researches will be also discussed. Finally, the challenges and future prospects of the field will be given.

4.2 Structure of Porous Anodic Aluminum Oxide (AAO) and Its Formation

Porous anodic aluminum oxide (AAO) film grown on aluminum has some structural analogy with a honeycomb (Fig. 4.1). It consists of a thin barrier oxide layer in contact with aluminum, and an overlying, relatively thick, porous oxide film containing mutually parallel cylindrical pores extending from the barrier oxide layer to the film surface. The thickness of porous AAO film can be varied from a few tens of nanometers up to hundreds of micrometers by controlling anodizing time. Each cylindrical pore and its surrounding oxide region constitute a hexagonal cell oriented normal to the metal surface. Under proper conditions, the oxide cells self-organize into hexagonal close-packed arrangement. Pore diameter and density of self-ordered porous AAOs are tunable in wide ranges by properly choosing anodizing conditions: pore diameter = 10–400 nm and pore density = 10^8 – 10^{10} pores cm^{-2} . The structure of self-ordered porous AAO can be defined by several structural parameters, such as interpore distance (D_{int}), pore diameter (D_{p}), barrier layer thickness (t_{b}), pore wall thickness (t_{w}), pore density (ρ_{p}), and porosity (P). These structural parameters have the following relationships [4]:

$$D_{\text{int}} = D_{\text{p}} + 2t_{\text{w}} \quad (4.1)$$

$$\rho_{\text{p}} = \left(\frac{2}{\sqrt{3}D_{\text{int}}^2} \right) \times 10^{14} \text{ cm}^{-2} \quad (4.2)$$

$$P(\%) = \left(\frac{\pi}{2\sqrt{3}} \right) \left(\frac{D_{\text{p}}}{D_{\text{int}}} \right)^2 \times 100 \quad (4.3)$$

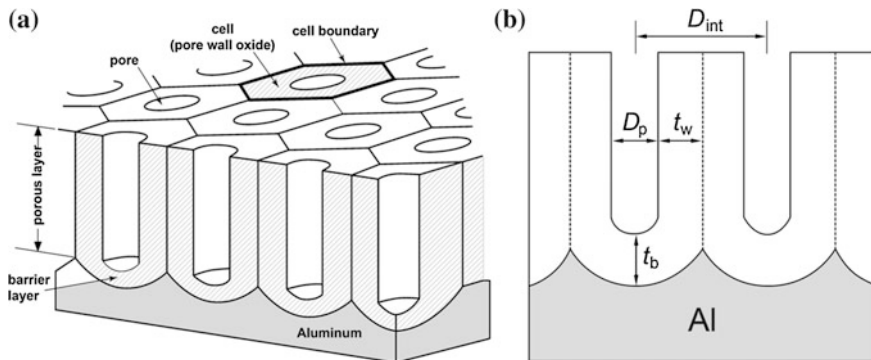


Fig. 4.1 Schematic structure of **a** porous anodic aluminum oxide (AAO) on Al substrate and **b** cross-sectional view; D_{int} = interpore distance, D_p = pore diameter, t_w = pore wall thickness, and t_b = barrier layer thickness

Studies to date have indicated that these structural parameters are dependent on the anodizing conditions, such as the type of electrolyte, anodizing potential (U), current density (j), temperature (T), etc.

During the formation of AAO films, the current (j) in the film is associated with the movement of charged ions in the barrier oxide layer, and can be described by the high-field conduction theory [14, 15]:

$$j = j_0 \exp(\beta E) = j_0 \exp(\beta U/t_b) \quad (4.4)$$

where j_0 and β are the constants, and U/t_b is the electric field (E , typically 10^6 – 10^7 Vcm^{-1}) impressed on the barrier layer with thickness t_b , the inverse of which is called “anodizing ratio (i.e., $AR = t_b/U$)” and describes the potential dependence of the barrier layer thickness. As such, the high-field conduction theory describes the field-driven movement of charged ions in barrier oxide. It is now well accepted that both Al^{3+} cations and oxygen-carrying anions (e.g., $\text{O}^{2-}/\text{OH}^-$) are mobile within the barrier oxide: Al^{3+} ions migrate outwardly toward the oxide/electrolyte (o/e) interface, while $\text{O}^{2-}/\text{OH}^-$ ions move inwardly toward the metal/oxide (m/o) interface [16–20]. In the case of barrier-type AAO formation, the cooperative counter movement of Al^{3+} and $\text{O}^{2-}/\text{OH}^-$ ions results in simultaneous formation of anodic oxide both at the o/e- and m/o-interfaces: at 100 % current efficiency, about 40 and 60 % of the total anodic oxide thickness is formed at the o/e- and m/o-interfaces, respectively [16–19]. On the other hand, in the case of porous AAO formation, anodic oxide forms at the m/o-interface by the inward migration of $\text{O}^{2-}/\text{OH}^-$ anions, while the outward migrating Al^{3+} cations are lost to the electrolyte through field-assisted direct ejection mechanism without contributing to the oxide formation [21–23]. Thus, current efficiency (η) in porous AAO formation is lower than that of barrier-type AAO formation.

Porous AAO can be prepared either under a constant potential (i.e., potentiostatic) or constant current (i.e., galvanostatic) condition using an electrochemical

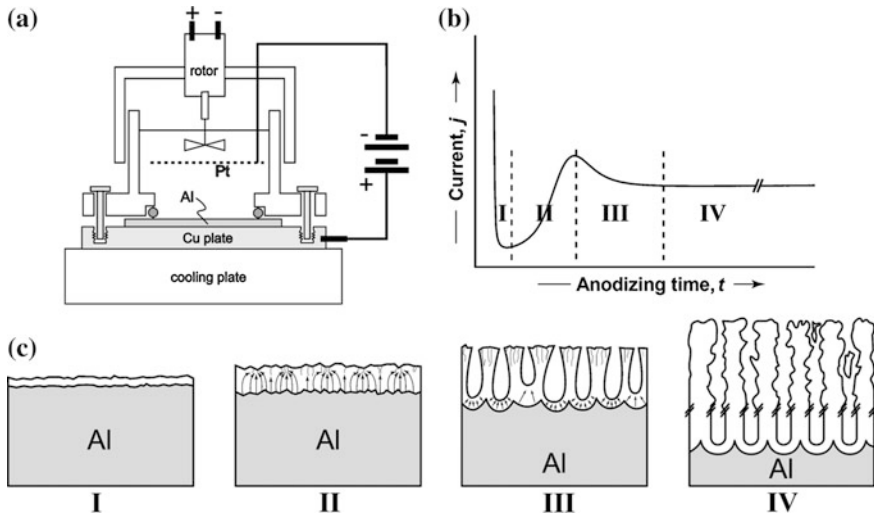


Fig. 4.2 Schematic diagram of **a** an electrochemical cell for typical anodization experiment, **b** a current (j)-time (t) transient during a potentiostatic anodization, and **c** the kinetics of porous AAO growth, corresponding to the anodization stages I-IV in panel (b)

setup shown in Fig. 4.2a. In general, potentiostatic anodization is widely employed for the fabrication of self-ordered porous AAO, because of the linear relation between the applied potential (U) and the structural parameters (i.e., D_p , D_{int} , and t_b) of the resulting AAO. Figure 4.2b, c illustrate a typical pore current (j)-time (t) transient in a potentiostatic anodization and the stages of pore structure development. Upon applying anodic potential, a thin compact barrier-type anodic oxide starts to grow on the surface of aluminum (stage I). When the thickness of compact barrier oxide reaches a certain value, current (j) drops rapidly to hit the minimum value. Electric field (E) may concentrate on local defects, impurities, or pits on the growing oxide surfaces to develop paths for electrolyte penetration, which serve as pore nucleation sites. Local field enhancement at the penetration paths facilitates field-assisted oxide decomposition, and leads to eventual development of incipient pores. Accordingly, further anodization leads to gradual increase in current (j) to a local maximum due to facile diffusion of electrolyte (stage II). At this stage, the pores are not uniform in size with random spatial distribution and undergo persistent merging with neighboring incipient pores to develop major pores (stage III). After that, current (j) reaches a steady-state value after passing an overshoot. During this state, gradual rearrangement of pores occurs over time until the field (E) across the barrier layers becomes the same for every pores (stage IV).

Several models have been explored to explain the formation of porous AAO. For steady-state pore growth, the velocity of the m/o- and o/e-interfaces should be balanced, keeping the barrier layer thickness (t_b) constant. This balance has long been attributed to an equilibrium between the oxide formation at the m/o-interface and the removal of oxide at the o/e-interface either by Joule's heat-induced

chemical dissolution [24–28] or by field-assisted oxide dissolution [26, 29–33]. But, recent studies have indicated that the dissolution-based pore formation model is operative for the initial stage of pore formation [34–36], whereas it does not adequately account for the steady-state pore formation. For steady-state pore growth, there is an increasing number of results from experiments and theoretical modeling, disproving the field-assisted oxide dissolution [23, 37–43]. The experimental evidences have been derived from the W-tracer studies by Skeldon and coworkers, who suggested that pores grow due to the viscous flow of oxide materials from the pore base toward the cell boundary under high electric field and growth stresses [23, 37–40]. The reader interested in this matter is referred to the recent review article given in [4].

4.3 Self-ordered Porous Anodic Aluminum Oxide (AAO)

4.3.1 Mild Anodization (MA)

Since early 1920s, various anodizing processes have been developed and extensively utilized by industry for the purpose of surface protection of aluminum products. But porous AAOs produced by industrial processes, represented by hard anodization (HA), are characterized by disordered structures with non-uniform pore shape, size, and spatial ordering. Therefore, the porous-type anodization processes have not been implemented in the nanotechnology research, until the discovery of self-ordered pore formation under mild anodization (MA) condition in 1995 [3]. MA is characterized by slow formation of porous AAOs due to the one- or two-orders of magnitude lower current density (j), compared to HA process. In their seminal work, Masuda and Fukuda found that long-term mild anodization (MA) of aluminum in 0.3 M oxalic acid ($\text{H}_2\text{C}_2\text{O}_4$) at 40 V leads to self-ordering of pores as a result of the gradual rearrangement of the initially disordered pores [3]. Based on this finding, Masuda and Satoh developed the so-called “two-step anodization” process, by which porous AAOs with highly ordered pore arrangement could be obtained [44].

Typical two-step anodizing process consists of (i) the first long-term anodization followed by removal of the resulting porous AAO layer with disordered pores in its top part (Fig. 4.3a) to obtain textured aluminum with arrays of almost hemispherical concaves (Fig. 4.3b) and (ii) the subsequent second-step anodization with the textured aluminum at the same condition used for the first-step anodization to obtain highly ordered pore arrangement (Fig. 4.3c). Typical porous AAOs formed by two-step MA process exhibit a polydomain structure, in which each domain contains hexagonally ordered defect-free pores and contacts with neighboring domains forming boundaries along which defect pores or imperfections in pore arrangement are present (Fig. 4.3d). The lateral size of individual domains increases with the anodizing time, but is limited to several micrometers.

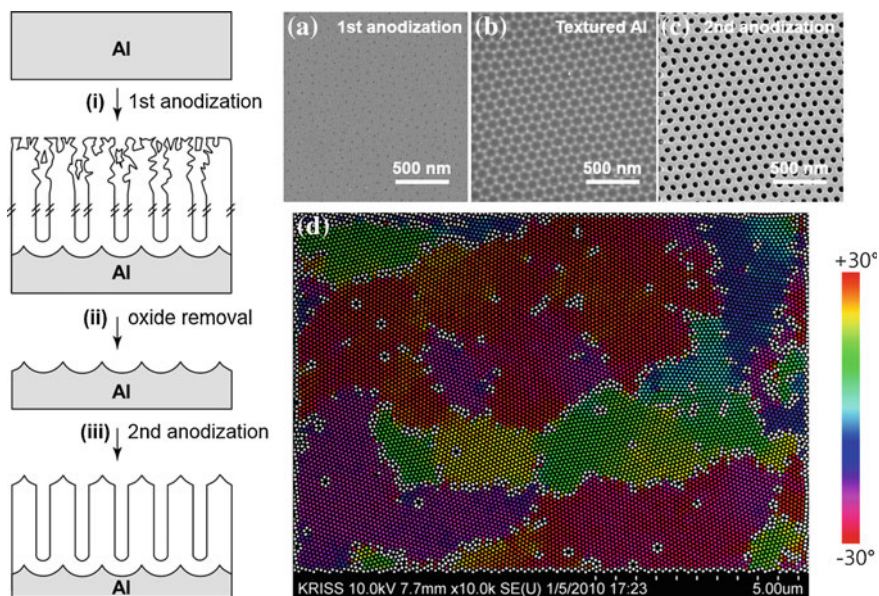


Fig. 4.3 *Left* A schematic procedure of a conventional two-step mild anodization (MA) for self-ordered porous anodic aluminum oxide (AAO): (i) the first long-term anodization step, (ii) removal of disordered porous AAO, and (iii) the second anodization step at the identical condition to the first one. **(a–c)** Representative plane-view SEM images of the samples of the respective steps. **d** A color-coded SEM image of AAO formed by two-step MA using 0.3 M oxalic acid at 40 V, showing a poly-domain structure. An area with the same color consists of a domain. The pores are color-coded on the basis of the average angle to the six nearest neighbors. Pores that have no apparent hexagonal coordination (i.e., defect pores) are marked with *white*

The development of the two-step process inspired and led to an overwhelming number of studies in attempts to fabricate ordered porous AAOs with different pore sizes and densities, to improve the spatial arrangement of pores, and to understand the mechanism of self-organized growth of pores. Particular efforts have been made to find the optimum pore ordering conditions for H_2SO_4 , $\text{H}_2\text{C}_2\text{O}_4$, and H_3PO_4 solutions, the electrolyte systems that were investigated by Keller et al. in the early 1950s [24]. Studies to date have indicated that for a given anodizing electrolyte there exists a narrow MA processing window (known as the “self-ordering regime”) leading self-organized growth of ordered pores (see Fig. 4.4): (i) sulfuric acid (0.3 M H_2SO_4) at $U = 25$ V for an interpore distance ($D_{\text{int}}^{\text{MA}} = 65$ nm [45, 46]; (ii) oxalic acid (0.3 M $\text{H}_2\text{C}_2\text{O}_4$) at 40 V for $D_{\text{int}}^{\text{MA}} = 103$ nm [27, 44–46]; (iii) selenic acid (0.3 M H_2SeO_4) at 48 V for $D_{\text{int}}^{\text{MA}} = 112$ nm [47]; and (iv) phosphoric acid (0.3 M H_3PO_4) at 195 V for $D_{\text{int}}^{\text{MA}} = 500$ nm [48, 49]. Considerable efforts have been devoted to exploring new self-ordering regimes in a wider range of interpore distance ($D_{\text{int}}^{\text{MA}}$). Most studies in this direction have been made by properly tuning the aforementioned three popular pore-forming acid electrolytes or by seeking new electrolyte systems. Shingubara et al. reported that anodization of aluminum in a

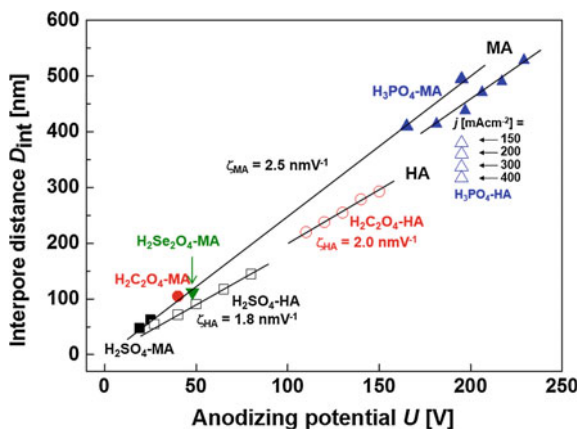


Fig. 4.4 Self-ordering regimes in MA (filled symbols) and HA (open symbols) by using H_2SO_4 (black), $\text{H}_2\text{C}_2\text{O}_4$ (red), H_2SeO_4 (green), and H_3PO_4 (blue symbols). The black solid lines are the linear regressions of the data with proportionality constants of $\zeta_{\text{MA}} = 2.5 \text{ nm V}^{-1}$ and $\zeta_{\text{HA}} = 1.8\text{--}2.0 \text{ nm V}^{-1}$. Reprinted with permission from [4]. Copyright 2014, The American Chemical Society

mixture solution of 0.3 M H_2SO_4 and 0.3 M $\text{H}_2\text{C}_2\text{O}_4$ (v/v = 1:1) yields self-ordered porous AAO with $D_{\text{int}}^{\text{MA}} = 73 \text{ nm}$ at $U = 37 \text{ V}$ [50]. Sun and coworkers have recently reported that the inter-pore distance can be continuously tuned from $D_{\text{int}}^{\text{MA}} = 410$ to 530 nm by anodizing aluminum in a mixture solution of H_3PO_4 and aluminum oxalate ($(\text{AlC}_2\text{O}_4)_2\text{C}_2\text{O}_4$) at $U = 180$ to 230 V [51]. About 50 years ago, Kape reported that organic acids containing at least two carboxyl ($-\text{COOH}$) group can act as anodizing electrolytes [52–54]. These acids include malonic, citric, tartaric, succinic, maleic, phthalic acid, and their mixtures of sulfuric or oxalic acid. Ono et al. have reported that porous AAOs with $D_{\text{int}}^{\text{MA}} = 300\text{--}600 \text{ nm}$ can be obtained by MA in some of these acid electrolytes: $D_{\text{int}}^{\text{MA}} = 300 \text{ nm}$ for 5 M malonic acid at 120 V , $D_{\text{int}}^{\text{MA}} = 500 \text{ nm}$ for 3 M tartaric acid at 195 V , and $D_{\text{int}}^{\text{MA}} = 600 \text{ nm}$ for 2 M citric acid at 240 V [55, 56]. Table 4.1 summarizes the self-ordering regimes for mild anodization (MA) of aluminum in some of pore-forming acid electrolytes.

It has been widely accepted that structural parameters of porous AAO formed under self-ordering regimes depend mainly on anodizing potential (U). The inter-pore distance ($D_{\text{int}}^{\text{MA}}$) and barrier layer thickness (t_{b}^{MA}) increase linearly with anodizing potential (U) with proportionality constants $\zeta_{\text{MA}} = 2.5 \text{ nm V}^{-1}$ for $D_{\text{int}}^{\text{MA}}$ and AR_{MA} (so-called “anodizing ratio”) = 1.2 nm V^{-1} for t_{b}^{MA} [46, 49, 58]. Pore diameter (D_{p}^{MA}) has also been known to increase with anodizing potential. However, recent studies have indicated that the potential dependence of D_{p}^{MA} is not as sensitive as the interplay between the current density and the temperature, concentration and nature of the anodizing electrolyte [47, 55, 59–61]. For MA-AAOs, Nielsch et al. proposed that self-ordering of pores requires a porosity (P_{MA}) of about 10 %, independent of the specific anodizing conditions by assuming $D_{\text{int}}^{\text{MA}} = 2.5 \text{ nm V}^{-1}$ [49].

Table 4.1 Self-ordering regimes for mild anodization (MA) of aluminum

Electrolyte	Self-ordering voltage, (U) (V)	Interpore distance, $(D_{\text{int}}^{\text{MA}})$ (nm)	$\zeta = D_{\text{int}}^{\text{MA}}/U$ (nm V ⁻¹)	References
0.3 M sulfuric acid H ₂ SO ₄	19–25	50–65	2.60	[45, 46]
0.3 M oxalic acid (HCOO) ₂	40	103	2.57	[27, 44–46]
0.3–3 M selenic acid H ₂ SeO ₄	42–48	95–112	2.26–2.33	[47, 57]
0.3 M phosphoric acid H ₃ PO ₄	160–195	420–500	2.63–2.56	[46, 48, 49]
5 M malonic acid HOOC–CH ₂ –COOH	120	300	2.50	[56]
3 M tartaric acid HOOC–(CHOH) ₂ –COOH	195	500	2.56	[56]
2 M citric acid HOOC–CH ₂ COH(COOH)CH ₂ –COOH	240	600	2.50	[55]

This requirement dictates a linear increase of the pore diameter (D_{p}^{MA}) with the anodizing potential at a rate of $\zeta_{\text{p}} = 0.83 \text{ nm V}^{-1}$, irrespective of anodizing conditions. On the other hand, there are a number of recent works, reporting that the self-ordering of pores can occur at other porosity (P_{MA}) values ranging from 0.8 to 30 % depending on the MA conditions [47, 55, 59–61]. For example, Nishinaga et al. have recently reported fabrication of porous AAO with porosity $P_{\text{MA}} = 0.8 \%$ ($D_{\text{p}}^{\text{MA}} = 10.4 \text{ nm}$ and $D_{\text{int}}^{\text{MA}} = 112 \text{ nm}$) by anodization of aluminum in 0.3 M H₂SeO₄ (0 °C) at 48 V [47]. The reported results clearly indicate that the anodizing potential is not the only parameter determining the pore diameter.

4.3.2 Hard Anodization (HA)

For a given anodizing electrolyte, there is a breakdown potential (U_{B}), above which stable anodization is difficult to maintain due to the commencement of local thickening, burning, and cracking of the growing oxide: $U_{\text{B}} = 27, 50,$ and 197 V for sulfuric, oxalic, and phosphoric acid, respectively. It has been known that breakdown of anodic oxide occurs due to the catastrophic local current flow and consequent Joule heating [4, 62–64]. Chu et al. reported that the best self-ordering of pores occurs when anodization is conducted at potentials just below the breakdown potential (U_{B}) [64]. Ono et al. have found that the locally thickened areas formed by breakdown exhibit domains of highly ordered cell arrangement [55, 65]. Further, they found that the interpore distance (D_{int}) and the barrier layer thickness (t_{b}) of porous AAO at the burnt areas are smaller than those at the burnt-free areas, which is consistent with the earlier results reported by Tu et al. [66]. All these results imply that at a given anodizing potential (U) current density (j) may determine the

spatial ordering of pores and the structural parameters (i.e., cell size D_{int} and the barrier layer thickness t_b) of porous AAOs.

Industrial hard anodization (HA) have been typically conducted at potentials higher than the breakdown value (U_B) [67–70]. HA-AAO films can be produced at an efficient rate (typically 50–100 $\mu\text{m h}^{-1}$) due to the high anodizing current at an increased anodizing potential [71–74]. The current density (j) in HA process is typically one or two orders of magnitude higher than that of conventional MA processes. Thus, Joule's heat (Q) during HA is two or four orders of magnitude greater than the ordinary MA processes: $Q = Ujt = R_b j^2 t$, where t is the anodization time and R_b is the resistance of the barrier layer. The excessive heat should be properly dissipated, otherwise it promotes dissolution and breakdown of the growing anodic oxide. The porous AAO films formed by industrial HA process are characterized by uneven surfaces with numerous cracks and non-uniform pores due to the local breakdown of anodic oxide, and thus are not suited to nanotechnology applications. Various attempts have been made to overcome the problems associated with the local breakdown events during HA. The researches in this direction include appropriate modifications of the three major pore-forming acid electrolytes (i.e., H_2SO_4 , $\text{H}_2\text{C}_2\text{O}_4$, and H_3PO_4), exploration of new anodizing electrolytes, and efficient removal of the reaction heat.

Chu et al. reported that the breakdown potential ($U_B = 27$ V) in a sulfuric acid-based anodization can be increased up to 70 V by ageing the electrolyte after a long-term pre-anodizing at 10–20 ampere hours per liter [64, 75]. The authors showed that self-ordered porous AAOs with $D_{\text{int}} = 90$ –130 nm at $U = 40$ –70 V and $j = 160$ –200 mA cm^{-2} at 0.1–10 °C. However, porous AAOs formed by this process exhibited poor mechanical stability due to weak cell junction strength, which would greatly limit their practical applications to current nanotechnology research. Chu et al. claimed that the concentration of Al^{3+} ions dissolved in an aged solution plays a key role in the stable growth of porous AAOs at high potentials ($U > U_B$) and current densities (j). But, later studies by Schwirn et al. have indicated that stable anodization at high potentials ($U > U_B$) is actually determined by the initial limiting current density (j_{limit}), not by the solution state [76, 77].

Lee et al. have shown that the self-ordering regimes can be extended by performing HA of aluminum in oxalic acid [78]. By introducing a thin (*ca.* 400 nm) porous oxide layer onto an aluminum substrate and effectively removing the reaction heat, they were able to prevent the breakdown of oxide films and grow mechanically stable ordered porous AAOs at anodizing potentials of $U > 100$ V [78]. Their HA process established a new self-ordering regime with widely tuneable interpore distances: $D_{\text{int}}^{\text{HA}} = 220$ –300 nm at $U = 110$ –150 V and $j = 30$ –250 mA cm^{-2} . They found that the porosity (P_{HA}) of HA-AAOs is 3.3–3.4 %, which is about one-third of the porosity value ($P_{\text{MA}} \approx 10$ %) that was proposed as a requirement for self-ordered MA-AAOs by Nielsch et al. [49]. The experimental method has also been applied to sulfuric and malonic acid-based HAs [77, 79].

Li et al. have reported that large reaction heat during HA can be effectively removed by adding ethanol ($\text{C}_2\text{H}_5\text{OH}$) to anodizing electrolytes, and thus can

achieve stable anodization at high potential ($U > U_B$) and current density (j) [80, 81]. The added ethanol served not only as an agent for lowering the freezing point of the electrolyte down to $-10\text{ }^\circ\text{C}$, but also as a coolant for the removal of reaction heat through its vaporization from the pore bases. The process allowed the fabrication of self-ordered porous AAOs with various interpore distances; $D_{\text{int}}^{\text{HA}} = 70\text{--}140\text{ nm}$ for $\text{H}_2\text{SO}_4\text{-HA}$ at $30\text{--}80\text{ V}$, $225\text{--}450\text{ nm}$ for $\text{H}_2\text{C}_2\text{O}_4\text{-HA}$ at $100\text{--}180\text{ V}$, and $320\text{--}380\text{ nm}$ for $\text{H}_3\text{PO}_4\text{-HA}$ at 195 V [80, 81].

Figure 4.4 shows the self-ordering potentials (U) and corresponding interpore distances (D_{int}) of porous AAOs formed by MA and HA in three major pore-forming electrolytes (i.e., H_2SO_4 , $\text{H}_2\text{C}_2\text{O}_4$, and H_3PO_4). HA-AAOs exhibit a reduced potential (U) dependence of the interpore distance (D_{int}) with a proportionality constant $\zeta_{\text{HA}} = 1.8\text{--}2.1\text{ nm V}^{-1}$ [75, 77–83], compared to self-ordered MA-AAOs (i.e., $\zeta_{\text{MA}} = 2.5\text{ nm V}^{-1}$). At a fixed anodizing potential, the interpore distance ($D_{\text{int}}^{\text{HA}}$) of HA-AAOs decreases with the current density (j), indicating that anodizing potential (U) is not the only parameter determining the cell size of HA-AAOs [77–80]. On the other hand, the barrier layer thickness (t_b) of HA-AAOs increases at a rate of $AR_{\text{HA}} = 0.6\text{--}1.0\text{ nm V}^{-1}$ with respect to anodizing potential (U) depending on the current density (j) [64, 77, 78, 80], which is smaller than $AR_{\text{MA}} \approx 1.2\text{ nm V}^{-1}$ for MA-AAO [24, 30, 84]. Lee et al. found that pore diameter (D_p) of HA-AAOs increases with current density (j) under potentiostatic conditions (i.e., $U = \text{fixed}$) (Fig. 4.5) [85]. Based on this observation, they suggested structural engineering of porous AAOs through appropriate control of the current density (j) during potentiostatic anodization.

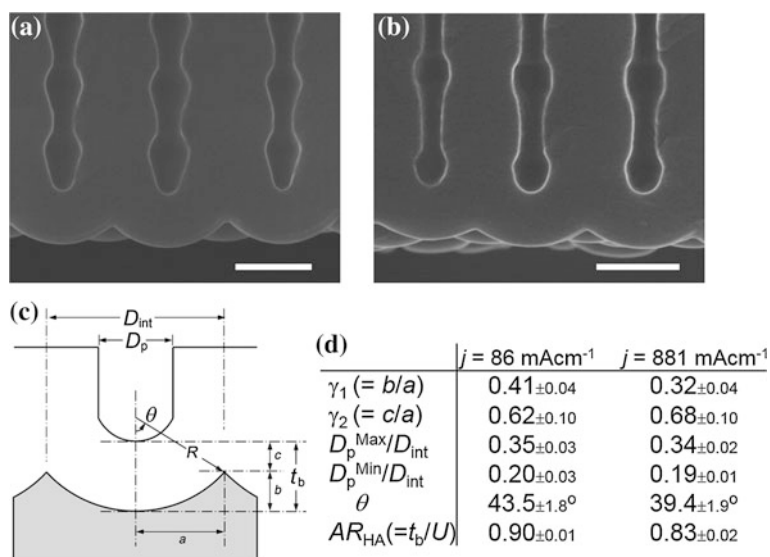


Fig. 4.5 Cross-section SEM micrographs of AAOs prepared from two separate anodisation experiments ($U = 200\text{ V}$), whose reaction were terminated near $j = 86\text{ mA cm}^{-2}$ and $j = 881\text{ mA cm}^{-2}$ in oscillating currents. Scale bars = 250 nm . **c** A schematic cross-section of AAO on Al. **d** The parameters defining the geometry of the pore bottom. Adapted with permission from [85]. Copyright 2010, WILEY-VCH Verlag GmbH & Co. KGaA, Weinheim

4.4 Structural Engineering of Porous AAO

4.4.1 Microstructuring of Porous AAO

The unique structural characteristics of the porous AAO make it not only an ideal template material for the preparation of arrays of nanodots, wires and tubes, but also an excellent platform material for the development of integrated nanodevices [4]. The elongated cylindrical feature of oxide pores can be exploited for the microstructuring of porous AAO films by anisotropic etching of the pore wall oxide. Tan et al. [86] demonstrated first the fabrication of high-aspect-ratio microstructures of porous AAOs by combining a conventional lithographic process and a wet-chemical etching process. For micromachining of porous AAO films, the same general process steps can be applied (Fig. 4.6a) [86–89]. First, a thin masking layer is patterned on the surface of AAO to selectively block the pores. Next, the resulting sample is immersed into an appropriate etching solution to selectively remove anodic oxide of the unmasked areas. During this process step, lateral etching of pore wall oxide takes place simultaneously along the entire length of the every unmasked pore, resulting in vertical side walls and negligible undercutting at the mask edges (Fig. 4.6b, c). Multilevel micromachining of porous AAO is also possible, as shown in Fig. 4.6d. After the first level microstructuring of AAO, the

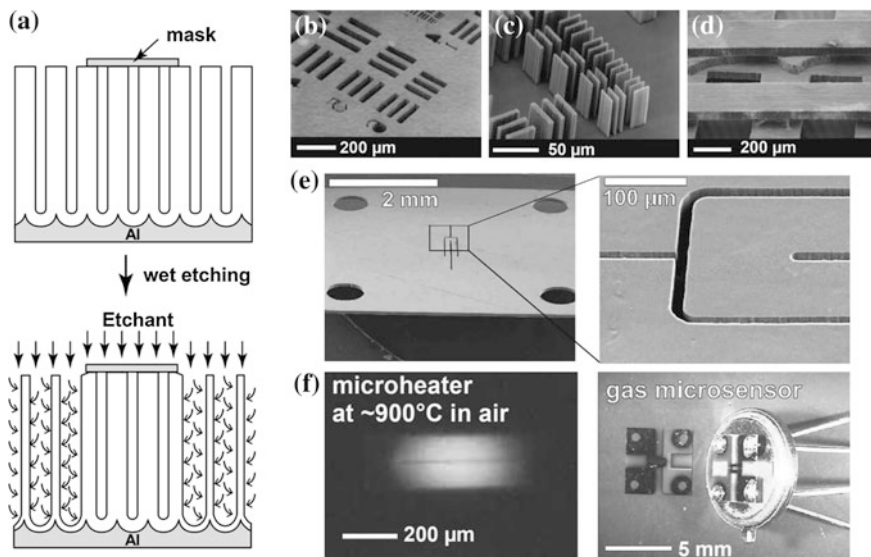


Fig. 4.6 a Scheme for the micromaching of porous AAO by anisotropic wet-chemical etching. b–d SEM micrographs of micromachined porous AAOs. e SEM micrographs of micromachined sensor substrate. f Device prototypes fabricated from micromachined porous AAO: microheater operating in air (left) and gas microsensor (right). Panels (b–f) adapted from [88]. Copyright 2000, American Society of Mechanical Engineers, ASME

remaining aluminum substrate can be further anodized. Afterwards, the newly formed porous AAO is patterned and etched similar to the first level micromachining.

Tan et al. [86] found that the time required for the complete removal of the unmasked areas is nearly independent of the thickness of porous AAO. This observation indicates that the process is governed by the oxide etching reaction, rather than the vertical diffusion of etching solution along the long cylindrical nanopores. Otherwise, the microstructures formed by etching would exhibit tilted sidewalls due to the etch rate difference between the top and bottom of pores. In other words, the critical thickness that must be etched corresponds to the pore wall thickness, rather than the film thickness of porous AAO.

In general, the pore wall oxide of as-prepared porous AAOs is amorphous and contaminated with the electrolyte-derived anionic impurity (see Sect. 4.4.3.1). Thus, porous AAOs exhibit poor chemical stability against both acid and base. But an amorphous AAO can be converted to polycrystalline alumina by proper heat treatment at high temperatures in air. The resulting porous alumina ceramic exhibits markedly improved hardness and chemical stability against acid, base, and other corrosive chemicals. Therefore, micromachined porous AAO can be used an excellent platform material for developing microelectromechanical system (MEMS) devices that operate even in high temperatures or harsh environments (Fig. 4.6e, f) [88, 89].

4.4.2 Control of the Arrangement and Shape of the Pores

As discussed in Sect. 4.3, self-ordered porous AAOs exhibit a poly-domain structure, in which each domain contains hexagonally arranged nanopores of an identical orientation (see Fig. 4.3d). The lateral size of ordered pore domains is typically limited to several micrometers. For advanced applications, on the other hand, porous AAOs with a single domain configuration of nanopores over macroscopic areas ($\sim \text{cm}^2$) are required. In addition, porous AAOs with non-hexagonal arrangement of pores or sharp-featured non-circular pore cross-sections may have extend application potential in biomedical sensors based on localized surface plasmon resonance (LSPR) or surface-enhanced Raman spectroscopy (SERS). The works in this direction was pioneered by Masuda and coworkers. They first reported the fabrication of porous AAOs with a single domain configuration of pores over a few mm^2 area [90]. The key of their method is to generate an array of shallow depressions on the surface of aluminum by mechanical nanoindentation with a hard SiC imprint stamp prior to anodization (Fig. 4.7a). Each surface depression on aluminum defined the position of pore growth during anodization, and thus led to a perfect hexagonal arrangement of pores within the stamped area (Fig. 4.7b). Masuda et al. further demonstrated fabrication of porous AAOs with square- or triangle-shaped pore openings in square or triangular arrangements (Fig. 4.7c, d) [91].

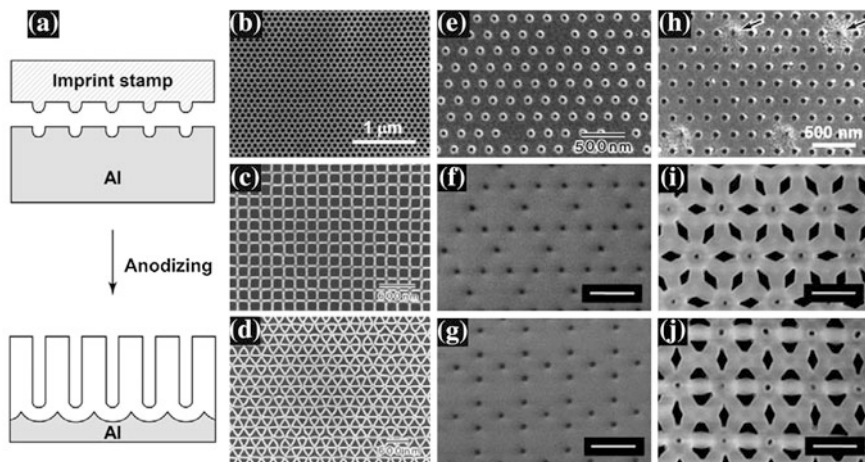


Fig. 4.7 **a** Schematic process for the preparation of an ideally ordered porous AAO by anodization of pre-patterned aluminum. **b–d** SEM micrographs of porous AAOs with different arrangements and shapes of pores: **b** circular, **c** square, and **d** triangular pore openings. **e–g** surface pre-patterns in non-equilibrium tessellation and **h–j** the respective porous AAOs formed by anodization. SEM images shown in (**f, g, i, j**) shows formation of porous AAOs with (**f, i**) hybrid circular-diamond and (**g, j**) hybrid circular-diamond-triangle pore cross-sections; the scale bars are 500 nm. Panel (**b**) adapted with permission from [90]. Copyright 1997, AIP Publishing LLC; Panels (**c, d**) adapted with permission from [91]. Copyright 2001, WILEY-VCH Verlag GmbH & Co. KGaA, Weinheim; Panels (**e, h**) reprinted with permission from [105]. Copyright 2001, AIP Publishing LLC; Panels (**f, g, i, j**) reprinted with permission from [106]. Copyright 2008, AIP Publishing LLC

To date, various strategies for surface pre-patterning of aluminum have been developed in order to generate surface pre-patterns either on bulk aluminum substrate or on thin aluminum layer deposited on fragile substrates (e.g., glass or Si wafer). These include imprinting with optical diffraction grating [92], lithographically fabricated Si_3N_4 [93] or Ni stamps [94], imprinting with self-assembled mono- or multi-layer of microbeads [95, 96], surface patterning by focused ion-beam (FIB) lithography [97–99], interference lithography [100], holographic lithography [101], block-copolymer lithography [102], step-and-flash imprint lithography (SFIL) [103], and soft lithography utilizing elastomeric poly-dimethylsiloxane (PDMS) stamp [104]. Each of these techniques has its advantages and disadvantages. The choice of the technique should be made in consideration of the process cost, the fragility of the substrate, the required size of single domain, etc. The reader interested in this matter is referred to the recent review article given in [4].

Masuda and coworkers found that in a pre-pattern on aluminum the deficiency sites of the pattern are compensated during anodization in order to achieve the closest packing configuration of the cylindrical cells (Fig. 4.7e, f) [105]. The size of the pores formed at the deficiency sites was smaller than that of pores formed at the patterned sites, which was attributed to the different pore growth rates at the

patterned and deficient sites [105]. Since the pore formation at the deficiency sites is associated with the establishment of the equilibrium tessellation arrangement of oxide cells, the anodizing potential (U) should be chosen to be the value that satisfies the potential (U)-interpore distance (D_{int}) relation required for the self-ordering of pores (see Sect. 4.3). By exploiting the self-compensation ability in AAO growth, Smith et al. have demonstrated the fabrication of porous AAOs with hybrid circular-diamond and circular-triangular-diamond pore cross-sections [106]. From anodizing experiments with Al surface pre-patterns in non-equilibrium tessellation arrangements (Fig. 4.7f, g), the authors found that the arrangement of the patterned and deficiency sites determines the cell geometry of the resulting porous AAO. On the other hand, the cell geometry was found to direct the shape of pores: circular, diamond, and triangular pores respectively in regular, elongated, and partially compressed hexagonal cells (Fig. 4.7i, j). It was suggested that a coupled effect between the thick pore wall oxide and the longer segment length of cell-boundary bands would account for the formation of diamond and triangular shaped pores [106].

4.4.3 Engineering of the Internal Pore Structure

4.4.3.1 Pore Widening

Pore wall oxide of as-prepared AAOs is amorphous and contaminated with varying amounts of anions derived from acid electrolyte. The incorporation of acid anions occurs via inward migrations under an electric field (E) during the anodization. The amount of incorporated acid anions and their spatial distribution in AAO depend on the type and concentration of electrolytes, anodizing potential (U), current density (j), and temperature (T) [28, 107–112]. The incorporated electrolyte anions influence the chemical, optical, and mechanical properties of porous AAOs. For instance, oxalate ions and the oxygen vacancies in AAOs formed in $\text{H}_2\text{C}_2\text{O}_4$ have been known to be the origin of the blue photoluminescences (PL) [81, 113–117]. In general, the pore wall oxide of AAOs exhibit a duplex structure in terms of chemical composition [108, 118–120]. The outer oxide layer next to the pores is contaminated with acid anions, yet the inner oxide layer is comparatively pure.

The duplex nature of the pore wall oxide can be conveniently evidenced by performing pore widening experiments. For a given set of pore widening conditions (i.e., temperature and concentration of an etchant solution), the rate of oxide etching is dependent on the chemical composition of the pore wall oxide [112]. Figure 4.8 shows the systematic increase in pore diameter (D_p) with the pore widening time (t_{etch}) for porous AAOs formed in H_2SO_4 , $\text{H}_2\text{C}_2\text{O}_4$, and H_3PO_4 . As shown in the figure, all D_p versus t_{etch} plots have the inflection points, at which the slopes of the curves change. Pore wall oxide in the early stage is etched at higher rates (ca. 1 nm min^{-1}) than those (ca. 0.37 nm min^{-1}) in the later stage. The retarded rate of etching in the later stage can be attributed to the relatively pure nature of the inner

pore wall oxide, compared to the less dense outer pore wall oxide due to the incorporation of acid anions. From the estimated inflection points, one can easily deduce the relative thickness ratios of the anion contaminated outer pore wall (t_o) to the more compact inner pore wall (t_i); they are summarized as an inset table in Fig. 4.8. The relative thickness of the outer pore wall (i.e., $t_o/(t_i + t_o)$) increases in the order:

$$\text{H}_2\text{SO}_4 - \text{AAO}(0.70) > \text{H}_2\text{C}_2\text{O}_4 - \text{AAO}(0.67) > \text{H}_3\text{PO}_4 - \text{AAO}(0.64)$$

From the view point of material's optical property, the pore wall oxide of AAOs have a trilayer structure [113, 115, 116]: (i) outer oxide layer contaminated with electrolyte anions (F^- -PL centers at 2.66 eV), (ii) middle oxide layer with singly ionized oxygen vacancies (F^+ -PL centers at 3.06 eV), and (iii) inner oxide layer (relatively pure alumina without PL centers). Yamamoto et al. [113] observed that pore widening treatment on porous AAO results in blue shift of the emission peak. They noted that the outer oxide layer screens the excitation light and the emission light from the middle oxide layer. Therefore, PL intensity increased initially with pore widening time (t_{etch}), but decreased upon oxide etching for an extended period of time due to the dissolution of the middle oxide layer.

Huang et al. reported that thin porous AAOs can act as a Fabry-Pérot optical cavity constituted by the air-AAO-AI, producing oscillating reflectance and PL spectra due to multiple-reflection interferences of the propagating waves [121]. From the fact that the band gap of alumina is much bigger than the photon energy of the considered PL spectral range (typically, 2.25–3.54 eV) and the absorption coefficient is very small, the authors deduced the optical thickness ($2nL_{\text{AAO}}$) of porous AAOs [121]:

$$2nL_{\text{AAO}} = hc/\Delta E \quad (4.5)$$

where n and L_{AAO} are respectively the refractive index and the thickness of a porous AAO, h and c are the Planck's constant (6.626×10^{-34} Js) and the speed of light (2.998×10^8 ms $^{-1}$), and ΔE is the mode spacing (i.e., the oscillation period) that determines the number of PL oscillations. The above equation predicts that the number of oscillations in a PL spectrum increases with the thickness (L_{AAO}) of porous AAO. From the laser-excited PL spectra of porous AAOs with different thicknesses, the authors estimated the refractive index of porous AAO to be $n = 1.66$ [121]. The refractive index (n) was about 2 % deviation to the effective refractive index ($n_{\text{eff}} = 1.62$) calculated from the Bruggeman's equation (4.6) assuming 8 % porosity (P) of porous AAOs [122]:

$$(1 - P) \frac{n_{\text{Al}_2\text{O}_3}^2 - n_{\text{eff}}^2}{n_{\text{Al}_2\text{O}_3}^2 + 2n_{\text{eff}}^2} + P \frac{1 - n_{\text{eff}}^2}{1 + 2n_{\text{eff}}^2} = 0 \quad (4.6)$$

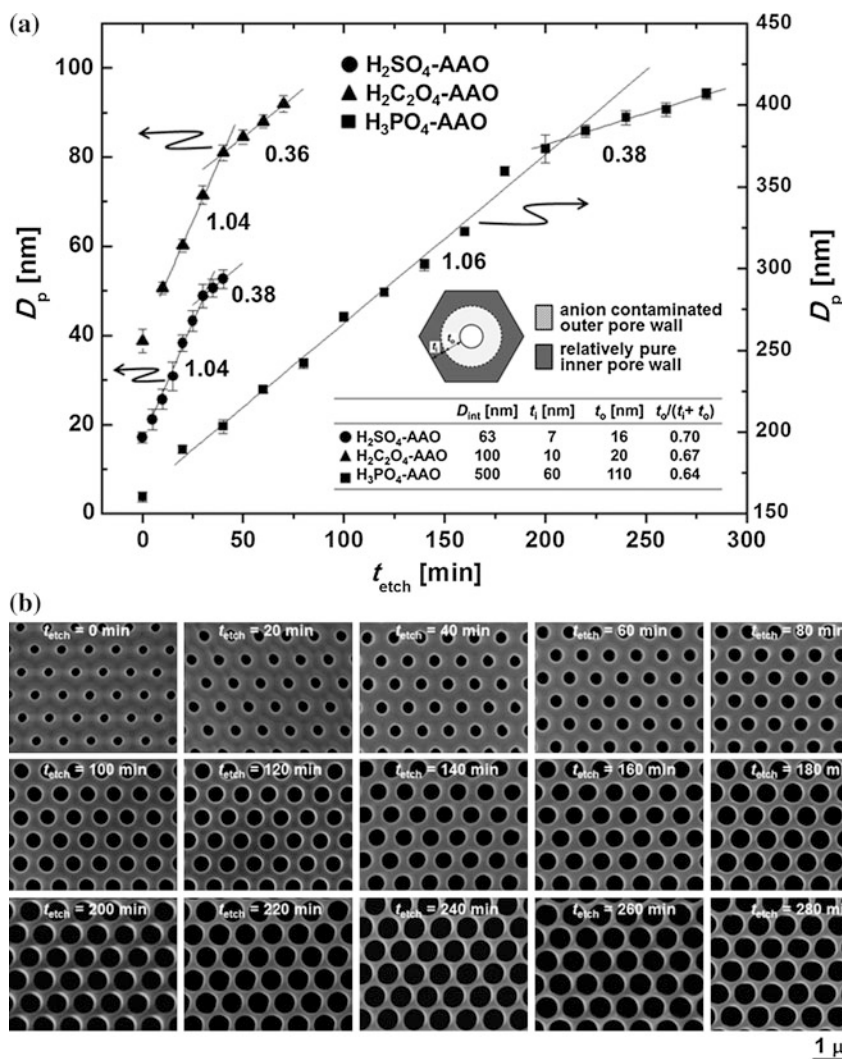


Fig. 4.8 The evolution of pore diameter (D_p) as a function of time (t_{etch}) upon wet-chemical etching of porous AAOs formed in 0.3 M sulfuric acid at 25 V (H_2SO_4 -AAO), 0.3 M oxalic acid at 40 V ($H_2C_2O_4$ -AAO), and 1 wt% H_3PO_4 at 195 V (H_3PO_4 -AAO). Wet-chemical etchings of pore wall oxide were performed in 5 wt% H_3PO_4 at 29 °C. The numbers in each plot are the slopes (in $nm\ min^{-1}$) of the corresponding linear fits. The table presented as an inset summarizes the relative thickness of the anion contaminated outer pore wall oxide layer (t_o) to the relatively pure inner pore wall oxide layer (t_i), which were determined from the inflection points of the D_p versus t_{etch} plots for three kinds of porous AAOs. **b** SEM images showing systematic increase in pore diameter (D_p) as a function of time (t_{etch}) upon wet-chemical etching in 5 wt% H_3PO_4 (29 °C). Data for $H_2C_2O_4$ -AAO were adapted from [112]

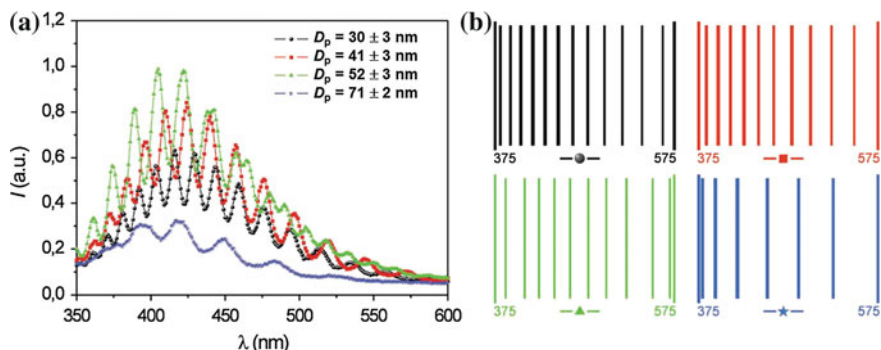


Fig. 4.9 **a** Photoluminescence (PL) spectra ($\lambda_{\text{ex}} = 320 \text{ nm}$) of porous AAOs with the same thickness ($t_{\text{AAO}} = 5.0 \pm 0.1 \text{ nm}$), yet different pore diameters (D_p). **b** The corresponding barcode patterns after encoding the measured PL oscillations in **(a)**. Adapted with permission from [123]. Copyright 2012 Wiley-VCH Verlag & Co. KGaA, Weinheim

where $n_{\text{Al}_2\text{O}_3}$ is the refractive index of alumina (1.67). Since the effective refractive index (n_{eff}) is a function of porosity (P), PL oscillation details can be tuned by changing the pore diameter (D_p) of porous AAO through pore widening treatment.

Santos and coworkers [123, 124] put forward the Fabry-Pérot effect to develop an optical encoding system based on the PL spectra of porous AAOs in the UV-Visible range (Fig. 4.9). Each PL oscillation corresponds to a bar in a barcode. The intensity and position of each PL oscillation are related to the width and position of each bar. As discussed above, the number, intensity and position of the PL oscillations depend on the thickness (L_{AAO}), pore diameter (D_p), and the nature of effective medium. By exploiting these features, the authors demonstrated that their barcode system can be used as optical biosensors for solvchromic oxazine molecules and glucose [123].

In an air-AAO-Al system, the wavelength of the peak maxima in a white light interference spectrum is governed by the Fabry-Pérot relationship:

$$2n_{\text{eff}}L_{\text{AAO}} = m\lambda \quad (4.7)$$

where λ is the wavelength of maximum constructive interference for spectral fringe of order m . The binding of molecules to the pore wall oxide gives rise to a shift of the characteristic interference pattern due to a change in the effective optical thickness (EOT, $2n_{\text{eff}}L_{\text{AAO}}$) that can be determined by the Fourier transform of the reflectivity spectrum. This analysis, so-called “the reflectometric interference spectroscopy (RIFS)” has been used by Sailor group for the investigation of gas adsorption characteristics within AAOs and also for label-free detection of bio-molecules [125–127]. More recently, Losic group has extended RIFS technique extensively for real-time detection of biologically relevant metal cations, volatile sulfur compound (VSC), and molecules [124, 128–131].

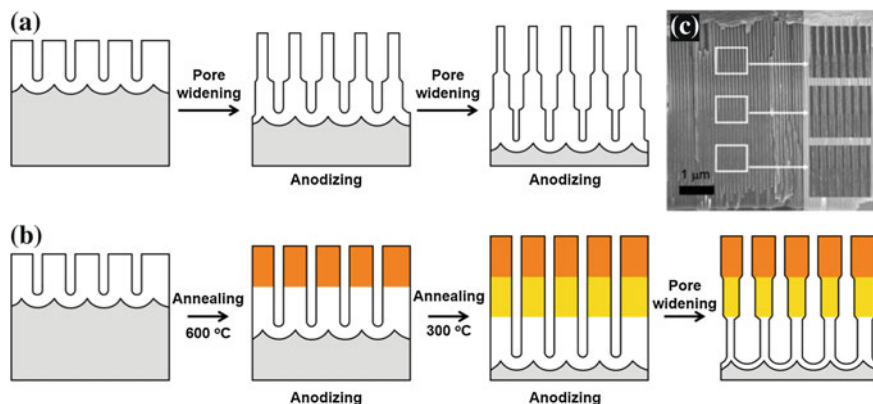


Fig. 4.10 Schematic procedures for the fabrication of porous AAOs with **a** normal and **b** inverted funnel-like pores: **a** combination of anodization steps and pore widening treatments in a sequential fashion and **b** combination of anodization steps and annealing treatments and final pore widening treatment. In (b), AAO strata after annealing at 600 and 300 °C are represented by *orange* and *yellow* colors, respectively. **c** Cross-sectional SEM micrograph of porous AAO with funnel-like pores prepared by the process (a). Panel (c) was reprinted with permission from [134]. Copyright 2007 The American Chemical Society

Pore widening treatment allows one to systematically increase the pore diameter (D_p) without affecting the interpore distance (D_{int}) of porous AAOs. This feature can be exploited in investigating the size dependence of physical properties (e.g., magnetic interaction) of low-dimensional nanostructures that can be fabricated by AAO template-based synthesis. Pore widening also offers a simple way of engineering the internal pore structure. For example, porous AAOs with funnel-like pores can be prepared by repeating the process comprised of anodizing and the subsequent pore widening treatment (Fig. 4.10a), in which the anodizing time and pore widening duration determine the length of each segment and pore diameter, respectively [132–134]. Li et al. have recently reported tailoring of the shape of funnel-like pores in AAOs [135]. The authors successfully demonstrated the fabrication of linear cones, whorl-embedded cones, funnels, pencils, parabolas and trumpets-like pore structures by controlling the anodizing time, pore widening time and cyclic time. Fabrication of inverted funnel-like pore structure has also been demonstrated recently by Santos et al. [136]. The approach was based on the different etching rate of pore wall oxide with the annealing temperature (Fig. 4.10b). Combination of two or more anodization steps and annealing at different temperatures after each anodizing step produced porous AAO strata having different chemical stabilities against etching solution. Pore widening treatment on the resulting porous AAO resulted in cylindrical pores with increasing pore diameter from top to bottom.

Funnel-shaped AAO pore structures have been used not only as sensing platforms, but also as templates to replicate optical nanostructures. Nagaura et al. fabricated porous AAO with low aspect ratio funnel-like pores and utilized it for

replicating ordered arrays of Ni nanocones by electroless Ni deposition [137, 138]. With similar approach, Yanagishita et al. replicated ordered arrays of tapered polymer pillars from funnel-like pores by photo-imprinting process and used it for investigating the effect of the tapering angle on the antireflection (AR) properties [139]. Among the polymer AR structures with various slopes (i.e., tapering angle), those with a gradually changing slope exhibited the lowest reflectance. He et al. [132, 134] showed that each segment of silica nanotubes prepared from AAO templates with funnel-like pores exhibit different light reflectance due to the diameter change along the length direction, allowing the identification of different shapes (i.e., codes) of nanotubes. Based on this optical reflectance property, the authors demonstrated that differently shaped silica nanotubes can be used as coding materials in a dispersible biosensor system [132]. In more recent study, Macias et al. showed that porous AAOs with funnel-like pores can be used for RfS-based label-free optical biosensing applications [140]. The authors prepared porous AAOs with two porous layers of different pore diameters (i.e., a top layer with large pores and a bottom layer with smaller pores (see Fig. 4.11a, b). The pore diameters of the

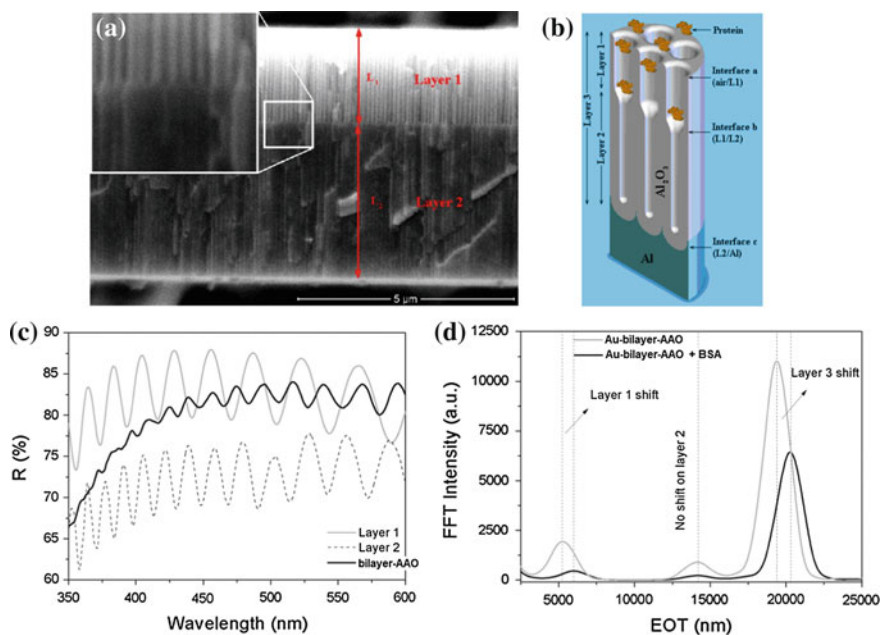


Fig. 4.11 **a** Cross-sectional SEM image of bilayered AAO. **b** Schematic of the sensing and self-referencing procedure, where the protein to be sensed can infiltrate Layer 1, but not Layer 2. Layer 3 = Layer 2 + Layer 2. **c** Reflectance spectra obtained from two single AAO layers and from a bilayer-AAO consisted of Layer 1 and 2: Layer 1 = 1.9- μm -thick and $D_p = 68$ nm (41 % porosity), Layer 2 = 4.7 μm -thick and $D_p = 33$ nm (9 % porosity). **d** FFT plot of the optical response of the Au coated-bilayer AAO before and after the introduction of the BSA protein. Adapted with permission from [140]. Copyright 2013, The American Chemical Society

top and bottom layers were designed for analyte (i.e., bovine serum albumin protein, BSA) to be infiltrated only into the top layer (i.e., L_1 in Fig. 4.11a), so that the bottom layer (i.e., L_2 in Fig. 4.11a) can serve as a self-reference, accounting for changes in the effective optical thickness that are caused by the medium of analyte. However, bilayered AAO exhibited non-periodic Fabry-Pérot oscillations with much reduced amplitude compared to L_1 - and L_2 -only AAOs due to the low refractive index contrast (Fig. 4.11c), which caused difficulties in the direct analysis of the top L_1 layer. In order to enhance the refractive index contrast between the top and both the bottom layer and the top incidence medium, a thin layer of Au was deposited on top of the porous AAO. This resulted in the appearance of the fast Fourier transform (FFT) peak corresponding to the top layer, otherwise barely visible, and in the amplified intensity of the peaks corresponding to the top layer as well as the whole bilayer structure (i.e., $L_1 + L_2$ in Fig. 4.11a). The amplified response translated upon analyte infiltration into a more sensitive determination of the change in the effective optical thickness (EOT) and in a much bigger change in the FFT peak amplitude ratios (Fig. 4.11d).

4.4.3.2 Potential Reduction

As discussed in Sect. 4.3, anodizing potential (U) determines the steady-state morphology of porous AAO. In other words, the barrier layer thickness (t_b), pore diameter (D_p), and interpore distance (D_{int}) of AAO are mainly determined by the potential (U). At a steady-state, the barrier layer thickness (t_b) remains constant due to the dynamic balance of the movement rates of the metal/oxide interface and the oxide/electrolyte interface. Thus, the current density (j) and the electric field ($E = U/t_b$) across the barrier layer are constant. When the anodizing potential (U_1) is reduced abruptly to the potential (U_2), the anodizing current (j) drops to a very small value due to the sudden decrease of the electric field (E), and after a certain period of delay it slowly increases to a steady value dictated by U_2 . This phenomenon has been known as “current recovery” and attributed to the thinning of the barrier layer accompanied by branching of pores [30, 141, 142]. Since the movements of ions (i.e., Al^{3+} and O^{2-}/OH^-) within the barrier oxide are governed by the electric field, the time required for complete current recovery increases with decreasing the field strength at the moment of potential drop [143, 144]. Porous AAO layer grown under a newly established steady-state exhibits reduced barrier layer thickness, pore size and spacing (i.e., increased pore density or porosity).

Furneaux et al. [145] reported that effective elimination of the barrier layer can be achieved by reducing anodizing potential in a series of small steps near to zero (Fig. 4.12). The authors suggested that the stepwise potential reduction maintains the electric field at a relatively high level and causes uniform thinning of the barrier layer. When the barrier layer was thin enough, porous AAO film was separated from the underlying Al substrate due to the dissolution of thinned barrier oxide by

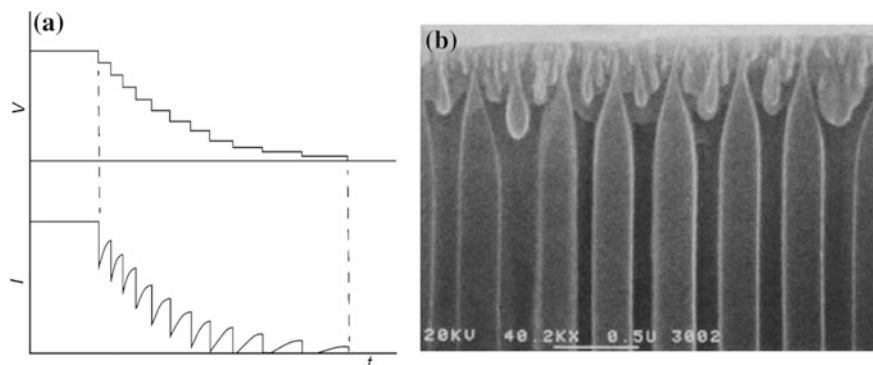


Fig. 4.12 **a** Schematic plots of voltage (V) and current (I) against time during the stepwise potential reduction process, where potential is stepped down, when the rate of current rise had fallen to 75 % of its maximum value. **b** Cross-section SEM image of porous AAO after the stepwise potential reduction process. Adapted with permission from [145]. Copyright 1989, Nature

the electrolyte. The resulting porous AAO film had an asymmetric membrane structure: larger straight pores extending through the bulk of membrane are interconnected with smaller branched pores which formed with a thin skin layer during the stepwise potential reduction process. Since the seminal work of Furneaux et al. [145], thinning of the barrier layer via stepwise potential reduction has been extensively exploited for template-based synthesis of various nanomaterials. It has been reported that the thinning may effectively reduce the potential barrier for the electrons to tunnel through the barrier layer, and thus allows alternating current (AC) electrodeposition of metallic nanowires into the pores of AAO that is attached on aluminum [146–149]. Free-standing AAO membranes obtained by stepwise potential reduction process have also been utilized for the preparation of metallic nanowires or multisegmented nanotubes by direct current (DC) electrodeposition [150, 151]. More recently, Jeon et al. [152] have demonstrated that AAOs with asymmetric membrane structure can be used as filters in enriching various fragile viruses in stocks without losing viral activity. For hepatitis c virus (HCV), the authors reported enrichment efficiency can be as high as 91 %, which is four times higher than that (~ 22 %) of conventional centrifuge-based technique. The origin of the efficiency enhancement was attributed to the perfect filtration of the virion particles without damage, whereas significant damage to the virions occurs during ultra-high speed centrifugation [152].

As mentioned above, potential reduction gives rise to branching of the primary pore channels. In general, pore branching is accompanied by random merging or dying of the newly generating pores, especially at the early stage of anodization at a reduced potential. Thus, it is rather difficult to define the pore structure at the oxide layer interconnecting the stem and branched pores. Considerable attention has been paid to control the pore branching behavior, since porous AAOs with tailor-made pore branches could be promising template materials for the synthesis various functional nanostructures with controlled levels of morphological complexity.

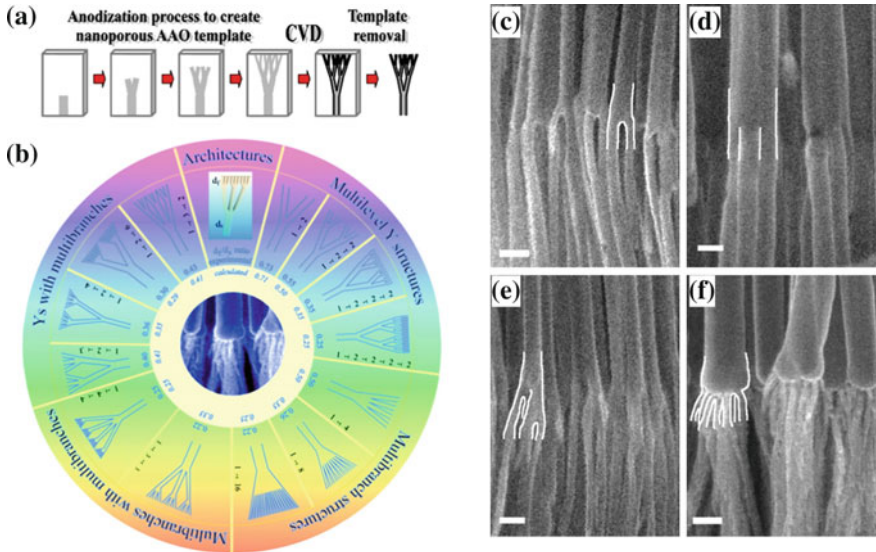


Fig. 4.13 **a** Schematic procedure for the preparation of carbon nanotubes (CNTs) having several hierarchical levels of multiple branching from AAO template with controlled porous architectures, where porous AAO is fabricated by consecutive steps of anodization, and then utilized as template to replicate CNTs by chemical vapor deposition (CVD). **b** Schematic showing CNT architectures that can be prepared from AAO templates with multiply branched pores. **c–f** SEM images of multiply branched CNTs showing the primary stem abruptly dividing into $n = 2, 3, 4$ and 16 branches, respectively (scale bars = 100 nm). Adapted with permission from [157]. Copyright 2005, The National Academy of Sciences of the USA

The work in this direction was first made by Li et al., who fabricated porous AAO with Y-branched pore channels by reducing anodizing potential by a factor of $1/\sqrt{2}$ [153]. Y-branched AAO pores have been utilized as templates for the preparation of Y-Junction carbon nanotubes (CNT) and metallic nanowires [153–156]. Later, Meng et al. expanded this work in order to fabricate multiply connected and hierarchically branched pores inside AAOs, of which hierarchical levels of multiple branching were represented by the notation $1 \prec n \prec m$, where “ \prec ” denotes the junction where the branching occurs, and “ n or m ” denotes the number of branched pores (Fig. 4.13) [157]. After the anodization for the stem pores in oxalic acid, the authors thinned the barrier layer prior to reducing the anodizing potential by a factor of $1/\sqrt{n}$. If the potential is lower than 25 V for pore branching, sulfuric acid was used instead of oxalic acid. Meng et al. claimed that the number and frequency of pore branching, dimensions, and the overall architecture of pore channels can be precisely controlled through properly designed potential reduction scheme [157].

In the works of Li et al. and Meng et al [153, 157], the potential reduction factors were chosen in consideration of (i) the linear dependence of the steady-state oxide cell dimension on the anodizing potential (i.e., $D_{\text{int}} = \zeta U$) and (ii) the invariance of the oxide cell area of a stem pore after branching; reducing the anodizing potential

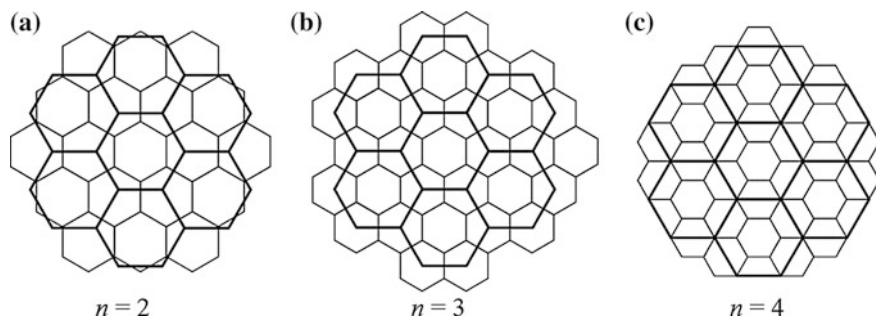


Fig. 4.14 Superposed hexagonal oxide cells. The area of larger oxide cells is **a** 2, **b** 3, and **c** 4 times that of the smaller cells. Panel **a** illustrates that the distribution of the Y-branched pores (i.e., $1 < 2$) cannot be close-packed. The extra space will cause splitting of the growing pore channels and result in a disordered and uncontrollable pore structure. Adapted with permission from [158]. Copyright 2009, The Royal Society of Chemistry

by a factor of $1/\sqrt{n}$ will produce n times as many smaller pores in order to maintain the original area of the oxide cell. However, this equal-area model for the growth of Y- or n -branched pore channels was argued by Shuoshuo et al. [158]. The authors claimed that it is impossible to control arbitrarily the growth of branched pore channels as a $1 < n$ structure, because the growth of some n -branched pores (e.g., $n = 2$; Y-branched pores) could not be a steady process and thus such branched pores could not be obtained uniform in a large scale. Based on theoretical consideration on the geometric arrangement of the branched pores, Shuoshuo et al. proposed that close-packed hexagonal arrangement of oxide cells can be achieved only for the potential reduction by the factors of $1/\sqrt{3}$, $1/\sqrt{4}$ and their common multiples and powers (i.e., $n = 3, 4, 9, 12, \dots$) (see Fig. 4.14); otherwise, the number of branched pores cannot be grown proportionally from each of the stem pores [158].

Non-steady-state formation of branched pores by potential reduction was systematically investigated by Ho and coworkers [159]. The authors fabricated three-dimensional (3D) two and three-tiered branched AAOs by stepping down anodizing potential for each anodizing step while thinning of the barrier layer is performed after each step; AAOs with the first tier having an average pore diameter of 285 nm branching into four 125 nm sub-pores in the second-tier and four 55 nm sub-pores in the third tier (Fig. 4.15a, b). They observed that the ratio of interpore distance (D_{int}) to the anodizing potential (U) of the second and subsequent tiers does not follow the characteristic constant value of $\zeta = 2.5 \text{ nm V}^{-1}$ for steady-state mild anodization (MA), but varies with an exponential function from $\zeta = 1.77$ to 1.26 nm V^{-1} when the potential ratio of the second- to the first-tier anodization changes from 0.5 to 0.96 (Fig. 4.15c). This difference was attributed to the constricted formation of the sub-pores by the boundaries of the preceding pores. On the other hand, the average number of sub-pores that can be generated within each preceding pore was observed to be decreased from 4.27 to 1.28 for the corresponding range of potential ratio (Fig. 4.15d).

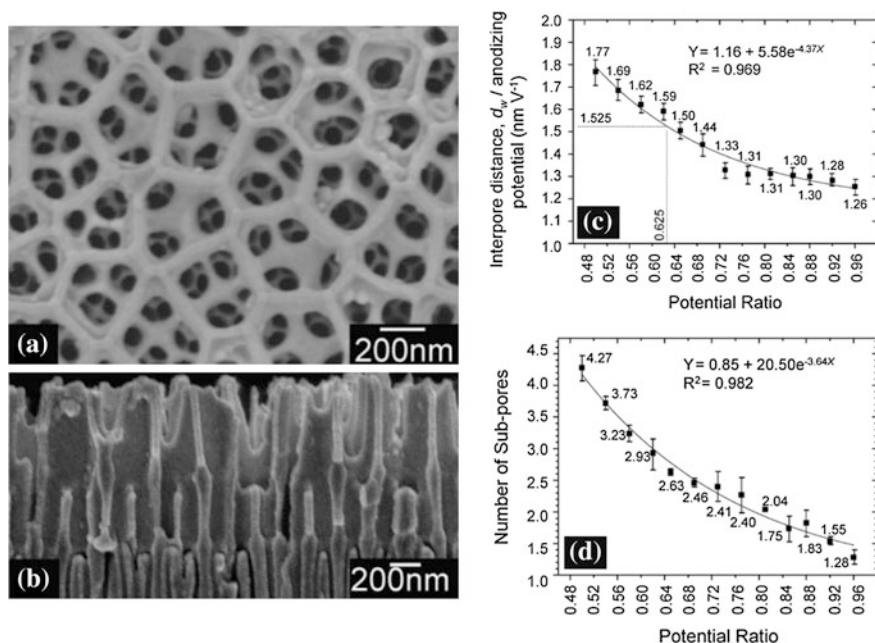


Fig. 4.15 **a** Top and **b** cross-sectional SEM images of AAOs with three-tiered branched pores prepared by multiple anodizations in 0.3 M H_3PO_4 (130 V), 0.15 M $\text{H}_2\text{C}_2\text{O}_4$ (80 V) and 0.15 M $\text{H}_2\text{C}_2\text{O}_4$ (80 V) followed by thinning of the barrier layer using 5 wt% H_3PO_4 . **c** Ratio of the sub-pores' inter-pore distance and anodizing potential ratio. **d** Number of sub-pores within each preceding pore versus anodizing potential ratio. Reprinted with permission from [159]. Copyright 2008 Wiley-VCH Verlag GmbH & Co. KGaA, Weinheim

4.4.3.3 Pulse Anodization (PA)

As discussed in Sect. 4.3.2, porous AAOs formed by hard anodization (HA) have one-third lower porosity (P) than those produced by mild anodization (MA) (i.e., $P_{\text{HA}} \approx 3\%$ for HA and $P_{\text{MA}} \approx 10\%$ for MA). Based on this experimental finding, Lee et al. [78] first demonstrated fabrication of highly ordered porous AAOs with periodically modulated pore diameters along the pore axes by properly combining MA and HA processes (Fig. 4.16). An ideally ordered porous AAO was first prepared by conducting MA in 0.4 M H_3PO_4 (10 °C) at 110 V. After that, the resulting sample was further anodized in an HA condition using 0.015 M $\text{H}_2\text{C}_2\text{O}_4$ (0.5 °C) at 137 V. Porous AAOs with periodically modulated pore diameters were obtained by repeating the above two anodization processes. The anodizing potentials (U) for MA and HA were chosen in consideration of the potential (U) and inter-pore distance (D_{int}) relations of the respective anodizing processes; $\zeta_{\text{MA}} = 2.5 \text{ nm V}^{-1}$ and $\zeta_{\text{HA}} = 2.0 \text{ nm V}^{-1}$. With a similar approach, Pitzschel et al. fabricated porous AAOs with modulated pore diameters using the same electrolytes yet under different anodizing conditions [160]. The resulting porous AAOs were used to prepare concentric $\text{SiO}_2/\text{Fe}_3\text{O}_4/\text{SiO}_2$ nanotubes by atomic layer deposition

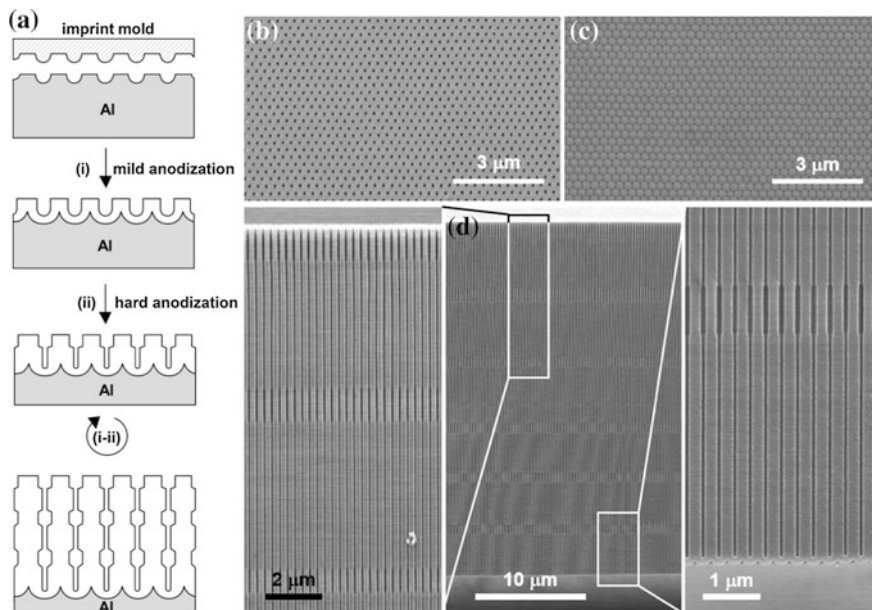


Fig. 4.16 **a** Scheme for the fabrication of porous AAO with modulated pore diameters by a combination of MA and HA. **b, c** SEM images of the *top* and *bottom* surface view of the porous AAO ($D_{\text{int}} = 275$ nm) formed by the process in **(a)**. **d–f** SEM images showing the cross-section view of the porous AAO with periodically modulated pore diameters. Reproduced with permission from [78]. Copyright 2006 Nature Publishing Group

(ALD) in order to investigate the effect of diameter modulations on the magnetic properties. In aforementioned approach, each step for pore modulation required a tedious manual change of the anodizing electrolytes and temperatures in order to satisfy both MA and HA processing conditions. Lee et al. have reported that this drawback can be overcome by performing pulse anodization (PA) of aluminum under potentiostatic conditions in sulfuric or oxalic acid electrolytes, demonstrating continuous structural and compositional engineering of porous AAOs (Fig. 4.17) [144].

In a typical PA process, a low potential (U_{MA}) and a high potential (U_{HA}) is alternately pulsed to achieve MA and HA conditions, respectively. A representative current-time (j - t) transient during PA of aluminum is shown in Fig. 4.17b. Current profile during a MA potential pulses is characterized by “current recovery” behavior (see the inset of Fig. 4.17b), similarly to the current evolution after potential reduction as discussed in Sect. 4.4.3.2: initially high current drops abruptly, hits a minimum value after a capacitive decay for a short time, and then gradually increases to reach a steady-state value after passing an overshoot. On the other hand, upon applying an HA pulse the current density (j) increases steeply for a short period of time and then decreases exponentially, which is the typical anodization

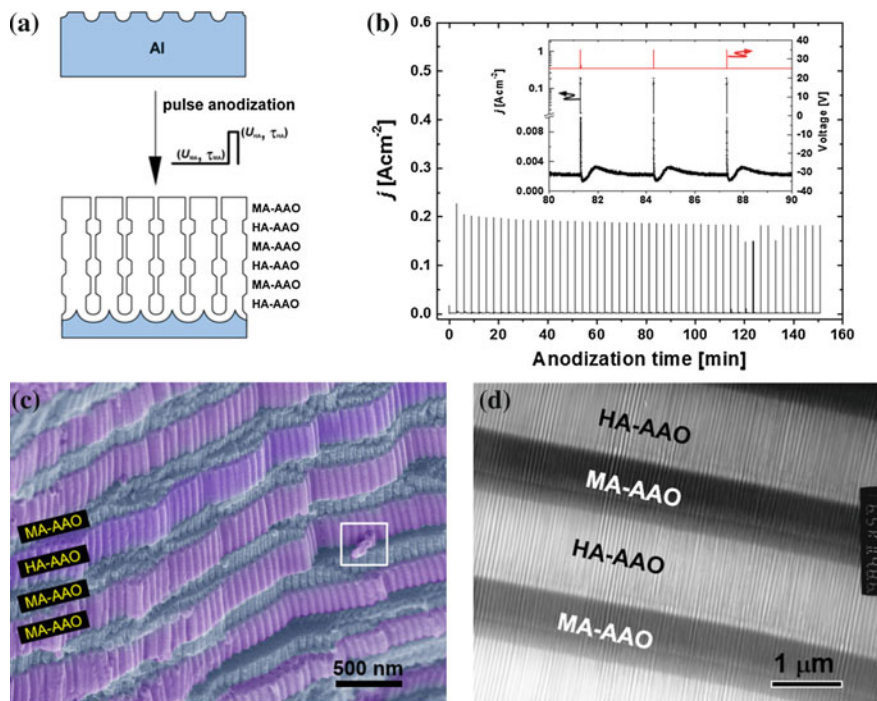


Fig. 4.17 **a** Scheme for the preparation of porous AAOs with modulated pore diameters by pulse anodization (PA). **b** A typical current-time (j - t) transient during PA of aluminium; pulses consisting of an MA pulse ($U_{MA} = 25$ V and $\tau_{MA} = 180$ s) followed by an HA pulse ($U_{HA} = 35$ V and $\tau_{HA} = 0.1$ s) were applied. *Inset* An enlarged j - t curve at $t = 80$ – 90 min. **c** False-colored SEM image of AAO formed by H_2SO_4 -PA. AAO slabs formed by MA and HA pulses are indicated by MA-AAO and HA-AAO, respectively. A white rectangle in (c) highlights alumina nanotubes (so-called “Keller-Hunter-Robinson cells”) that were separated from the nearby HA-AAO slab. **d** Cross-sectional TEM image of AAO formed by pulse anodization using 0.3 M H_2SO_4 ($U_{MA} = 25$ V, $\tau_{MA} = 180$ s, $U_{HA} = 37$ V, $\tau_{HA} = 1$ s), showing image contrast in MA- and HA-slabs due to the difference in pore diameter. Reproduced with permission from [144]. Copyright 2008 Nature Publishing Group

kinetics of potentiostatic HA of aluminium [78]. As shown in Fig. 4.17b, current density (j) changes periodically to the values dictated by pulsed potentials (i.e., j_{MA} for U_{MA} and j_{HA} for U_{HA}). As a result of periodic variations of current amplitude, the resulting porous AAO exhibits a layered structure with alternate stacking of MA-AAO slab with a smaller pore diameter and HA-AAO slab with a larger pore diameter (Fig. 4.17c, d). The thickness of each oxide slab is determined by the pulse durations (i.e., τ_{MA} for MA-pulse and τ_{HA} for HA-pulse). As a characteristic feature of porous AAOs formed by pulse anodization in sulfuric acid (i.e., H_2SO_4 -PA), MA-AAO and HA-AAO slabs exhibit different fracture behaviors against external

stresses (Fig. 4.17c). For MA-AAO slabs, cracks propagate through the center of pores from pore to pore. For HA-AAO slabs, on the other hand, the cracks develop along the cell boundaries and not through the center of the pores, indicating fairly weak cell junction strength. Cleavage through the cell boundaries in AAO formed by HA pulses resulted even in single Al_2O_3 nanotubes or bundles of tubes (so-called “Keller-Hunter-Robinson cells”) [24, 161, 162].

Apart from periodic modulations of pore diameter, Lee et al. found that the change of the current amplitude during PA results in periodic compositional modulation of the resulting AAO along the pore axes. Their microscopic elemental analysis of porous AAO formed by sulfuric acid-based PA indicated that the content of electrolyte-derived impurities (mostly SO_4^{2-}) in HA-AAO slabs is about 88 % higher than in MA-AAO slabs, which was attributed to the high current density (j_{HA}) during HA-pulsing (typically, $j_{\text{HA}} \approx 10\text{--}10^2 \times j_{\text{MA}}$) [144]. In general, anodic oxide contaminated with anionic impurities is labile to chemical attack of an oxide etchant (e.g., 5 wt% H_3PO_4). Therefore, a periodic compositional modulation in pulse anodized AAO may result in an etching contrast between MA- and HA-AAO pore wall oxides, allowing the fabrication of porous AAOs, in which the difference in the pore diameters of HA- and MA-AAO is pronounced than in as-prepared samples. Upon wet-chemical etching of pore wall oxide, pulse anodized AAO exhibits a structural color that is tunable by controlling the pulse durations (i.e., τ_{MA} and τ_{HA}). By taking advantage of poor chemical stability of HA-AAO slabs against an oxide etchant, Lee et al. [144] could completely separate the entire MA-AAO slabs from a single as-prepared porous AAO by selectively etching HA-AAO slabs (Fig. 4.18). The thickness of MA-AAO slabs could be varied from a few hundred nanometer to several micrometers by changing MA pulse duration (τ_{MA}). This demonstration indicated that PA of aluminum and wet-chemical etching of the resulting porous AAO could be a simple, continuous, and economic way for the mass production of porous AAO sheets.

As mentioned above, when the anodizing potential is changed from a higher U_{HA} to a lower U_{MA} , the current density drops abruptly from j_{HA} to a minimum value and then increases gradually to a value (j_{MA}) corresponding to U_{MA} (i.e., current recovery). It was reported that the time required for a complete recovery of anodizing current depends on the chemical nature of the barrier oxide (i.e., the content of anionic impurities), the electrolyte temperature, and the potential difference between U_{HA} and U_{MA} (i.e., the electric field strength at the moment of potential drop): For three popular anodizing electrolytes, it increases with the order $\text{H}_2\text{SO}_4 < \text{H}_2\text{C}_2\text{O}_4 < \text{H}_3\text{PO}_4$ [143, 144]. Unlike H_2SO_4 -based PA, PA of aluminum in $\text{H}_2\text{C}_2\text{O}_4$ or H_3PO_4 electrolyte is difficult to achieve continuously within a reasonable period of time because of the retarded current recovery, especially at a low temperature and a large potential difference [143, 144]. In order to solve the problem associated with the slow current recovery, Lee and Kim increased gradually anodizing potential prior to pulsing a high anodizing potential [143]. By

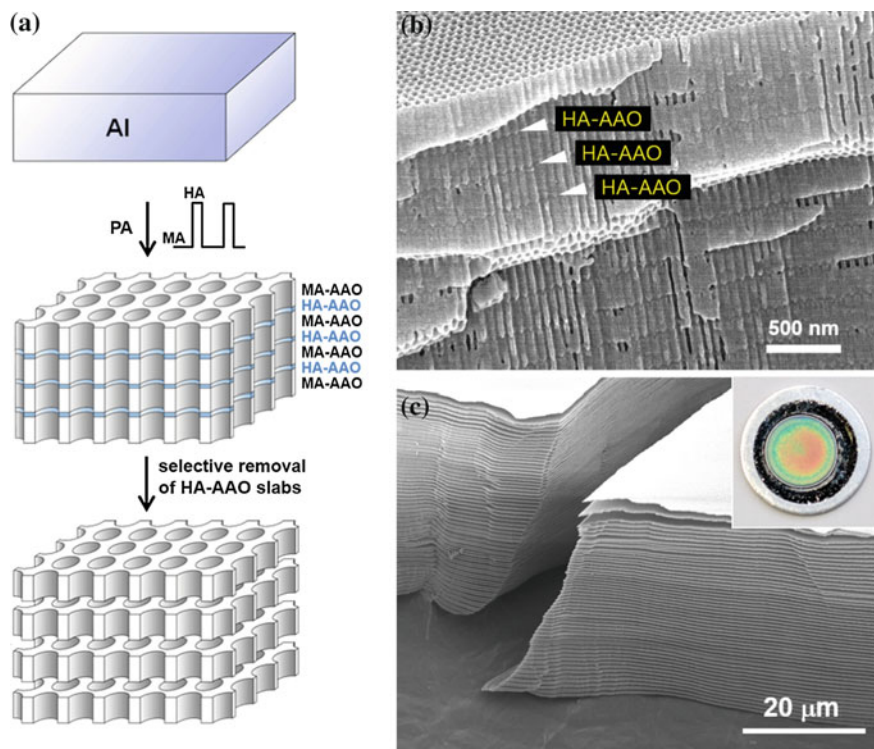


Fig. 4.18 **a** Scheme for the mass production of porous AAO membranes by a combination of pulse anodization (PA) and wet-chemical etching. **b, c** SEM images of porous AAO formed by PA and stacks of MA-AAO slabs after selective removal of HA-AAO slabs by wet-chemical etching. The inset of **c** shows a photograph of pulse anodized AAO on aluminum after wet-chemical etching treatment. SEM images were reproduced with permission from [144]. Copyright 2008 Nature Publishing Group

employing potential pulses with specifically designed periods and amplitudes, they successfully demonstrated engineering of the internal pore geometry (Fig. 4.19), enabling fabrication of optically active 3D porous architectures and also expanding the degree of freedom not only in AAO-based synthesis of functional nanowires and nanotubes with modulated diameters.

Structural modulation of porous AAOs can also be achieved by galvanostatic PA, where current pulses satisfying MA and HA conditions are periodically applied. As mentioned above, HA-AAO slabs formed by H_2SO_4 -PA shows weak junction strength between cells. By exploiting this feature, Lee et al. [163] developed a convenient route for the mass preparation of uniform anodic alumina nanotubes (AANTs) with prescribed lengths. They applied periodically galvanic MA and HA pulses to achieve continuous modulations of pore diameter and also to weaken the

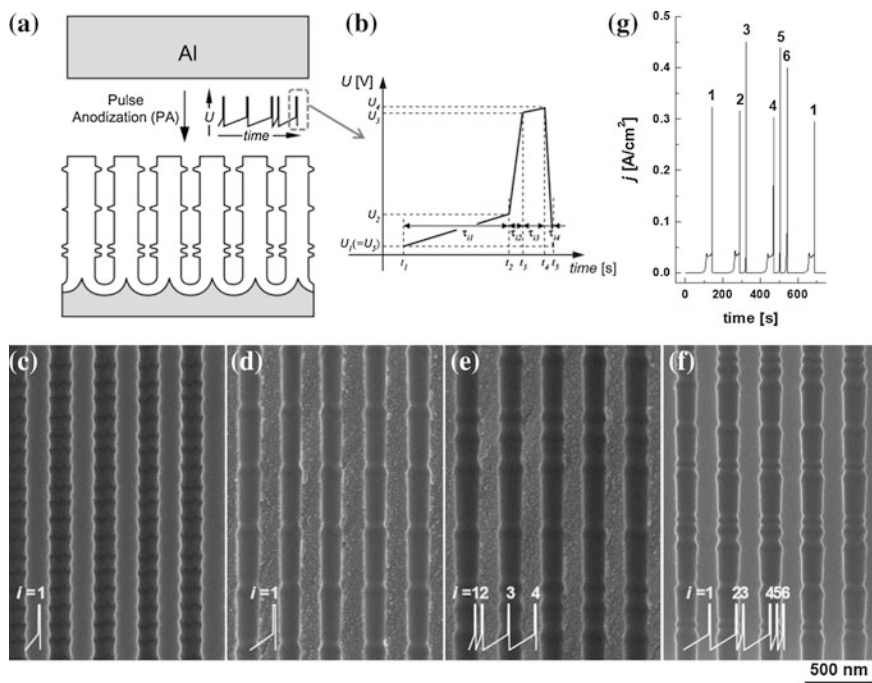


Fig. 4.19 Schematics showing **a** the experimental process for the fabrication of AAO with tailor-made pore structures by pulse anodization (PA) and **b** a generalized form of a potential pulse employed in pulse anodizations. U_j and τ_{ij} define the repeating unit of potential waves, where $U_j =$ the potential at the time t_j with $U_1 = U_5$ ($j = 1-4$), $\tau_{ij} = t_{j+1} - t_j$, $i =$ the pulse number ($i = 1, 2, 3, \dots$). Representative SEM image of porous AAOs with modulated pores prepared by pulse anodization; **c** $\tau_{11} = 36$ s, **d** $\tau_{11} = 144$ s, **e** $\tau_{11} = \tau_{21} = 36$ s, $\tau_{31} = t_{41} = 144$ s, and **f** $\tau_{11} = \tau_{21} = 144$ s, $\tau_{31} = 36$ s, $\tau_{41} = 144$ s, $\tau_{51} = \tau_{61} = 36$ s. Other parameters were fixed at $U_1 = 80$ V, $U_2 = 140$ V, $U_3 = U_4 = 160$ V, $\tau_{12} = \tau_{14} = 0$ s, $\tau_{13} = 0.2$ s. The repeating units of potential pulses are shown as insets in the respective images. **g** Current (j)-time (t) transient for the sample shown in **(f)**. From [143]. Copyright 2010 IOP Publishing

junction strength between oxide cells. AANTs, the length of which is determined by the HA-pulse duration (τ_{HA}), could be obtained by immersing the resulting porous AAO into an acidified CuCl_2 solution, followed by ultrasonic treatment in order to release individual oxide nanotubes from the as-anodized sample (Fig. 4.20). Uniform AANTs with controlled length may merit various applications because of material's excellent physicochemical properties, including a large effective surface area, high dielectric constant, chemical inertness, and biocompatibility [164–167]. Recently, Logic group have demonstrated that AANTs formed by galvanostatic PA can be used as new drug delivery nanocarriers by using tumor necrosis factor-related apoptosis-inducing ligand (Apo2L/TRAIL) as a model drug Fig. 4.21) [168].

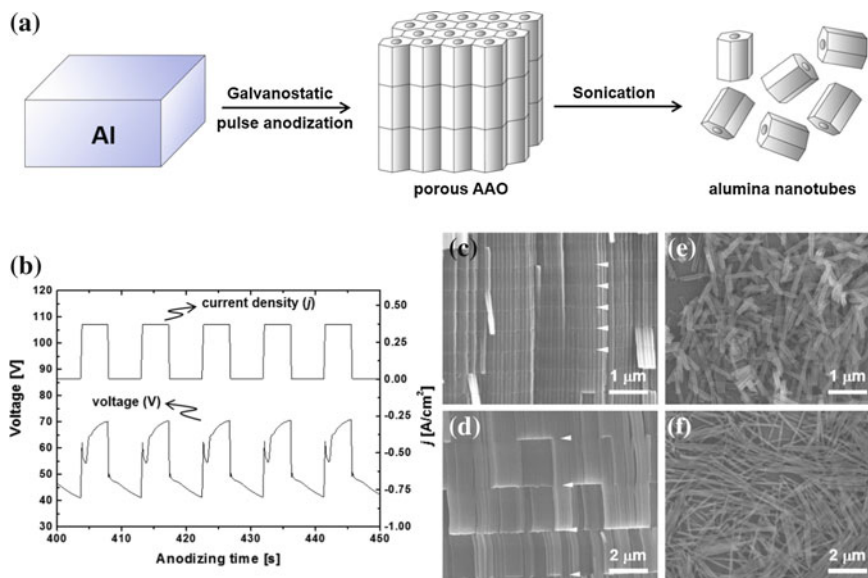


Fig. 4.20 **a** Scheme for the mass production of Al_2O_3 nanotubes with prescribed lengths. **b** A typical current (j)-voltage (V) relation during galvanostatic pulse anodization (PA) of aluminum. **c**, **d** Cross-sectional SEM micrographs of AAOs formed by galvanostatic PA: $\tau_{\text{HA}} = 2$ s for (**c**) and $\tau_{\text{HA}} = 6$ s for (**d**). Other pulse parameters were fixed at $j_{\text{HA}} = 368.42 \text{ mA cm}^{-2}$, $j_{\text{MA}} = 3.16 \text{ mA cm}^{-2}$ and $\tau_{\text{MA}} = 5$ s. **e**, **f** SEM micrographs of Al_2O_3 nanotubes obtained from the sample shown in panel (**c**) and (**d**), respectively. Reprinted with permission from [163]. Copyright 2008 The American Chemical Society

Their study have shown that as-prepared AANTs exhibit ultra-high pro-apoptotic protein Apo2L/TRAIL loading capacity ($104 \pm 14.4 \mu\text{g mg}^{-1}$), and provide a successful release with considerable local concentration ($>24 \mu\text{g}$) at in vitro simulated physiological condition. The effectiveness of AANTs-Apo12L/TRAIL nanocarriers was confirmed by effective reduction in viability of MDA-MB231-TXSA breast cancer cell, which was attributed to the cell apoptosis induced by high concentration of Apo2L/TRAIL loaded in AANTs.

An approach for pore modulations without combination of MA and HA processes has been reported by Santos et al. [169]. The process, so-called “discontinuous anodization (DA)”, uses potential pulses under MA regime and thermally activated oxide dissolution condition [169]. In this method, self-ordered porous AAO was first grown by anodizing a textured aluminum in 0.3 M H_3PO_4 (1 °C) at 170 V. After 6 min, anodizing was stopped and the electrolyte temperature was increased to 35 °C. After that, DA process was started. DA consisted of applying consecutive MA pulses ($U_{\text{MA}} = 170 \text{ V}$ and $\tau_{\text{MA}} = 1 \text{ min}$) separated each other by a designated relax period ($U_{\text{relax}} = 0 \text{ V}$ and $\tau_{\text{relax}} = 3, 6, 9, \text{ or } 12 \text{ min}$). The modulated pores of the resulting AAOs changed from a slender node-like, ellipsoidal, and

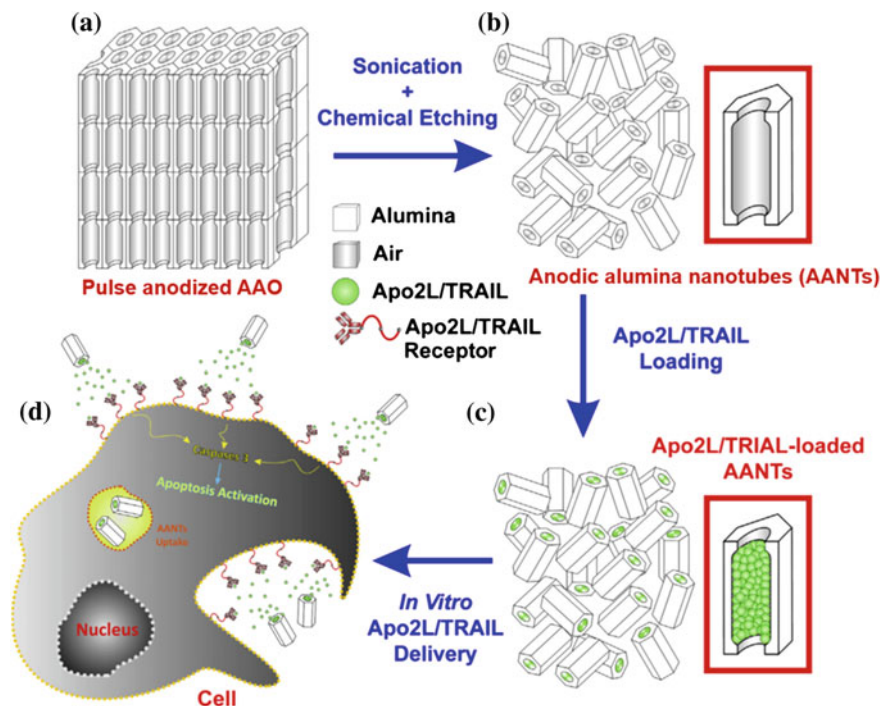


Fig. 4.21 Schematic illustration showing application of anodic alumina nanotubes (AANTs) for in vitro drug delivery of tumor necrosis factor-related apoptosis-inducing ligand (Apo2L/TRAIL). Adapted with permission from [168]. Copyright 2014 Elsevier Ltd

asymmetric serrated morphology depending on the relax period. It was proposed that the generation of the pore modulations is associated with the formation of a gel-like layer (e.g., $\text{Al}(\text{OH})_3$) during the period of relax and its subsequent detachment during the beginning of each potential pulse [169]. The proposed mechanism appears to explain the experimental observations. But it should be supported by the evidence that can confirm the presence of gel-like layer on the entire surfaces of the pores. It was reported that gel-like material on pore wall surface is very soluble in acid electrolytes even at room temperature [85]. Gel-like layer on the pore wall surface may be formed by re-deposition of dissolved oxide species within the pores, which typically occurs upon drying of an improperly rinsed porous AAO. Santos et al. [169] attributed the sharp increase in anodizing current (j) at the beginning of each potential pulse to the detachment of the gel-like layer from the pore base. But, an alternative interpretation can be made for this observation as follow: During the period of relax, acidic dissolution of pore wall oxide would occur due to the high electrolyte temperature, thus pores are enlarged. Simultaneously, the barrier layer is thinned. As a consequence, anodizing current

(j) increases steeply upon applying MA pulses but decreases almost exponentially to steady-state value as the pores grow with their equilibrium morphology. The reported maximum current density (j) upon MA pulses was about 40 mA cm^{-2} , which is about 10 times higher than that of typical H_3PO_4 -MA at comparable temperature. The high current density (j) at the beginning of each potential pulse would account for observed pore modulation. In fact, it has been reported that at a given anodizing potential (i.e., $U = \text{constant}$) pore diameter (D_p) increases with current density (j) [85].

4.4.3.4 Cyclic Anodization (CA)

Losic et al. put forward the concept of structural engineering of internal pore structures of AAO by combining MA and HA [170]. They developed a new anodization process, termed “cyclic anodization (CA)”, which is based on slow and oscillatory changes of the anodizing conditions from MA to HA regimes. The authors used periodically oscillatory current signals with different profiles, amplitudes, and periods in order to achieve pore modulations in porous AAOs (Fig. 4.22). By applying current signals of different cyclic parameters, porous AAOs with different pore shapes (circular- or ratchet-type), lengths, periodicity and gradients were prepared. Microscopic investigation on the samples indicated that the internal pore geometry is directed by the characteristics (i.e., profile, period, and amplitude) of the applied cyclic signal. The authors pointed out that the transitional anodization (TA) mode, the transition from MA to HA regime, is important for structural engineering of pores in their CA process; the minimum current of the applied cycle is responsible for the formation of the smallest pores (MA), the slope in the current directs the main pore shape (TA), and the maximum current is responsible for the formation of the largest pores. The authors further demonstrated fabrication of porous AAOs with distinctive, hierarchical internal pore structures by employing multiprofiled current signals; for example, three different successive CA steps, beginning with first cycle having a gradually increasing amplitude of current, then a double-profiled cycle, and lastly a series of triangular galvanic cycles. In a separate report, the same authors demonstrated fabrication of porous AAOs with laterally perforated pores (i.e., pores with nanoholes along horizontal directions) by a combination of CA and wet-chemical etching of the resulting porous AAOs [171].

As mentioned in Sect. 4.4.3.3, porous AAOs with periodically modulated pore diameters may exhibit colors, when their modulation period is the order of the visible light wavelength. In other words, porous AAO with appropriately modulated pores can behave like a distributed Bragg reflector (DBR) that consists of periodically stacked layers of different refractive indices, reflecting a range of wavelengths propagating in the direction normal to the stacked layers. The range of wavelengths that are reflected is called the “photonic stopband”. The central wavelength of stopband depends on the refractive index and the layer thickness. On the other

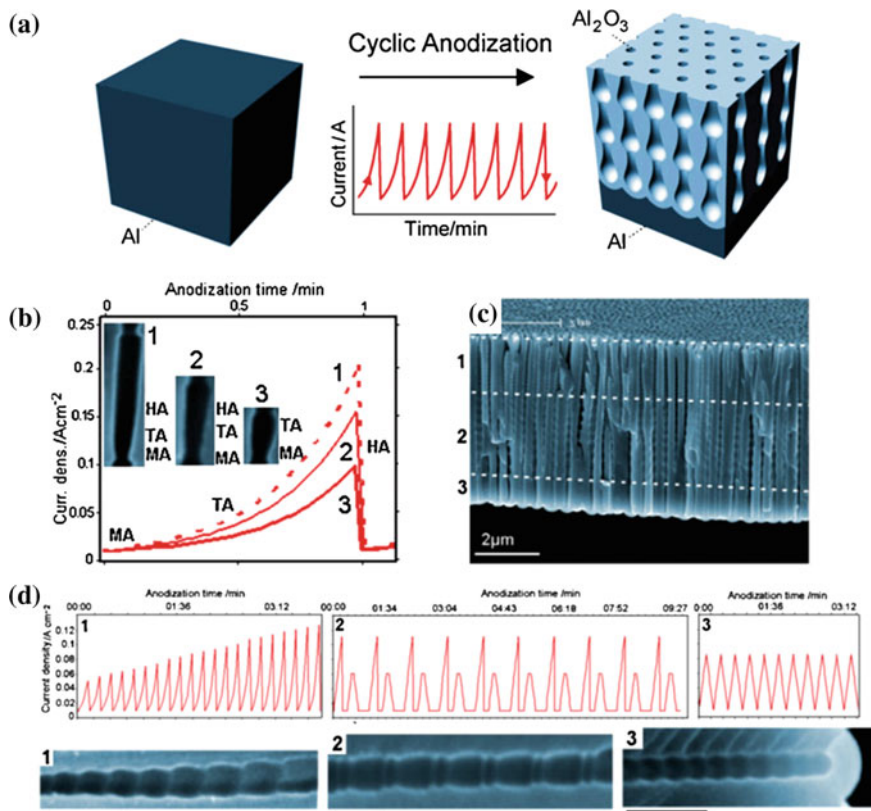


Fig. 4.22 **a** Schematics of the galvanostatic cyclic anodization (CA). **b** Influence of current amplitude on the pore shape and the length of modulated pore segments. Anodization modes (i.e., MA, TA, HA) associated with corresponding anodization currents are marked on the pore structures and graphs. **c** SEM image of porous AAO with multilayered pore architectures and different pore modulation patterns. **d** Current profiles versus pore geometries of the sample shown in (c). Scale bars = 500 nm. Reprinted with permission from [170]. Copyright 2009 Wiley-VCH Verlag GmbH & Co. KGaA, Weinheim

hand, its bandwidth depends on the refractive index contrast, the relative layer thickness within one period, and the total number of layers. Due to its outstanding optical characteristics, DBRs have been important components in various optoelectronic devices (e.g., vertical cavity surface-emitting laser, reflector mirrors, electroabsorptive reflection modulators), and thus cheap and robust ways of realization of DBR structures have been intensively explored recently [172–174].

Optical properties of structurally engineered porous AAOs have been intensively investigated by Fei group [175–180]. They first reported that photonic crystals made of “air pores” in AAOs can be fabricated by applying periodically varying

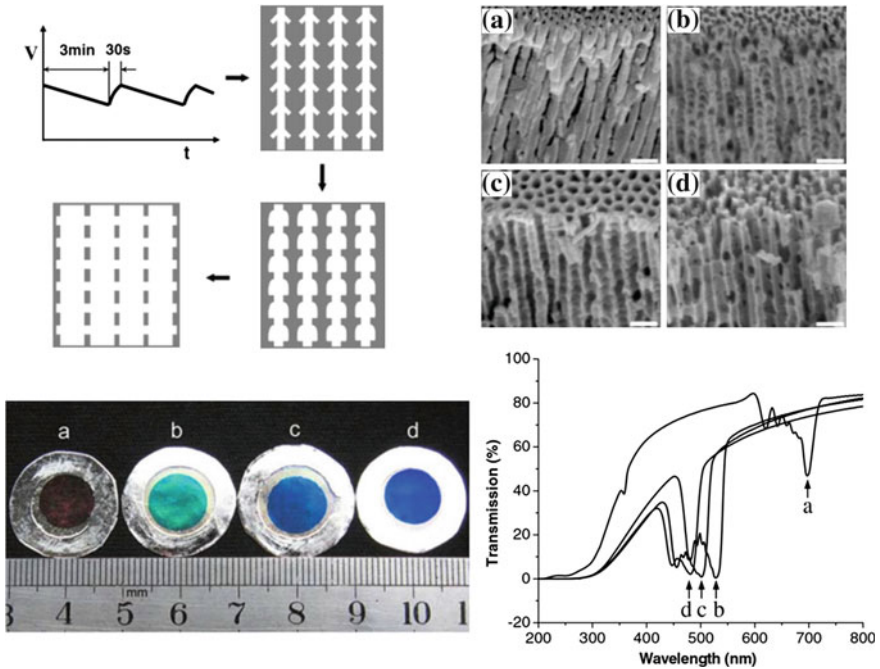


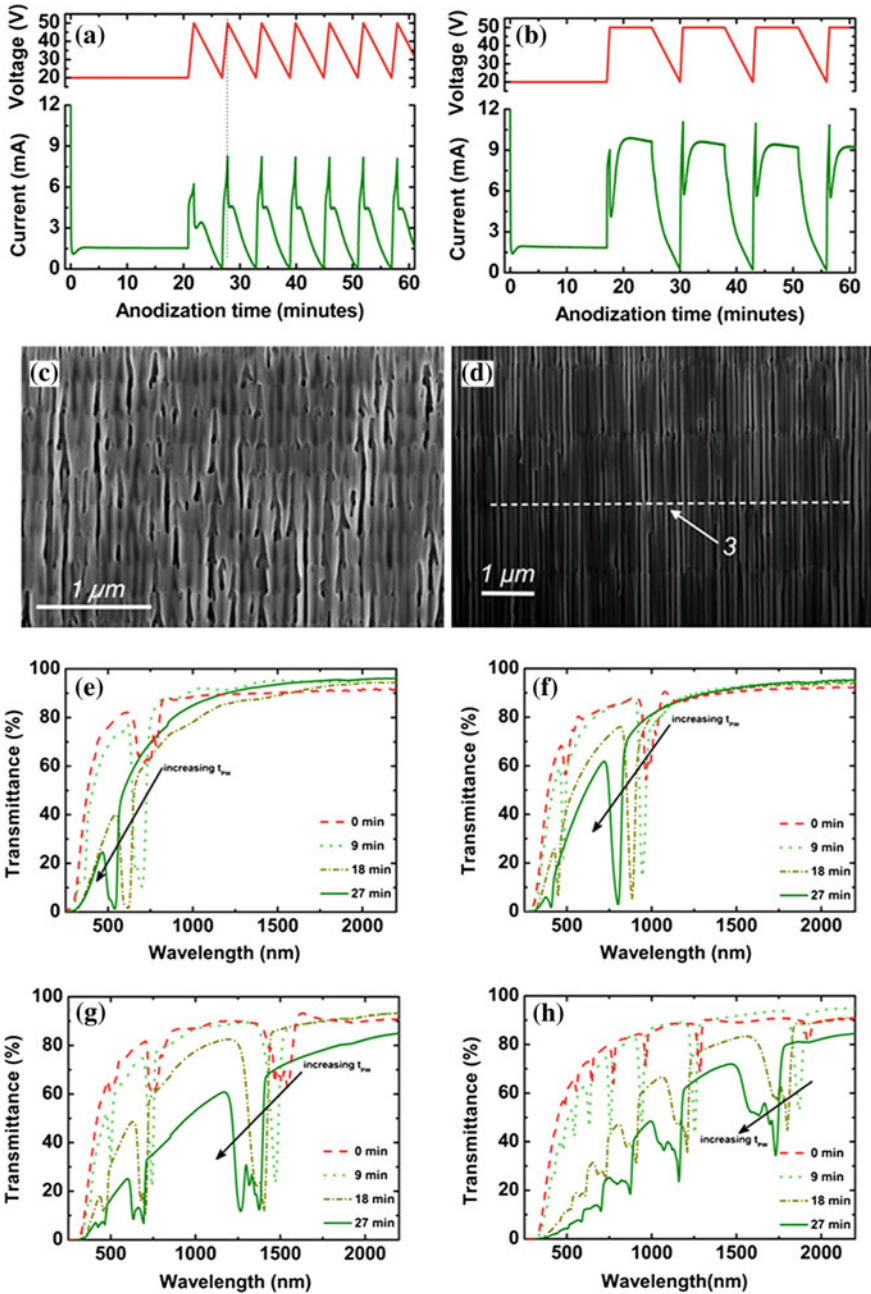
Fig. 4.23 *Top-left* Schematic procedure for the fabrication of a photonic crystal made of air pores in AAO by a combination of anodization of aluminum with periodically changing potential and wet-chemical etching. *Top-right* SEM images of porous AAO (a) before and after chemical etching for **b** 15 min, **c** 18 min, and **d** 20 min. Scale bars = 200 nm. *Bottom-left* A photograph and *Bottom-right* transmission spectra of the corresponding samples. Adapted with permission from [175]. Copyright 2007 IOP Publishing

potential during anodizing and subsequently performing wet-chemical etching of the resulting AAOs (Fig. 4.23) [175]. For anodization of aluminum, anodizing potential was linearly decreased from 53 to 23 V in 3 min, and then increased from 23 to 53 V in 30 s. Straight main channels were formed during the high-potential duration, and each main channel branched into several small channels during the low-voltage duration. By cycling this process, a periodic structure with main and branched channels could be formed. The stopband position in the transmission spectra could be controlled in the range from 450 to 525 nm by adjusting the time for wet-chemical etching. Later, the same group of authors put forward their approach in order to fabricate AAO-based DBR structures and demonstrated that the first Bragg condition for the main inhibition of incident light perpendicular to the surface of AAO can be modulated from 727 to 1200 nm by modifying waveform of anodizing potential [176]. With a separate report, they also showed that the transmission spectra of AAO-based DBRs can be modulated further to cover almost any wavelength range of the visible light by simply modifying the anodizing

temperature [177]. The effect of incidence angle on the optical properties of AAO-based DBRs was studied by Xing et al. who observed that when the incidence angle increases progressively, a blue shift of the transmission peak occurs with gradual decrease of the peak intensity [181]. Fei group has recently demonstrated that structurally engineered porous AAOs can be used as gas sensors [178, 179]. Porous AAOs were prepared by using so-called “voltage compensation mode”, which was claimed to effectively compensate the unevenness of the pore size caused by ion concentration decrease at the pore bottoms and the pore wall dissolution by the electrolyte [178, 180]. Porous AAO behaved as photonic crystal with an ultra-narrow photonic bandgap (PBG), of which the full width at the half maximum is only 30 nm. Based on shift of PBG upon exposure to ethanol vapor, porous AAO-based photonic crystal gas sensor was fabricated.

More recently, Ferré-Borrull group reported that an in-depth modulation of the pore geometry and the refractive index of AAO-based DBRs can be achieved by potentiostatic CA of aluminum with deliberately designed potential cycles (Fig. 4.24) [182]. For the modulation of pores, 150 potential cycles were applied, in which each cycle consisted of three phases: (i) a linear increasing potential ramp from 20 to 50 V at a rate of 0.5 Vs^{-1} , (ii) an interval of constant potential at 50 V lasting for time to flow a given charge ($Q_o = 0, 0.5, 1$ and 4 C), and (iii) a linearly decreasing potential ramp from 50 to 20 V at 0.1 Vs^{-1} (Fig. 4.24a–d). After the anodization process, wet-chemical etching of the resulting porous AAOs was carried out using 5 wt% H_3PO_4 (35°C) in order to increase pore diameters for different period of times (0, 9, 18, and 27 min). Transmittance spectra of the AAO-based DBRs revealed that by controlling the amount of charge involved in each cycle it is possible to modulate the photonic stopband position from the UV to the near-infrared range. Further, the pore-widening causes blue shift of the stopbands and modifies their width and depth (Fig. 4.24e–h). The study well demonstrate the ability to control the photonic stopband by modulating the refractive index contrast between the layers through a combination of CA and controlled pore-widening.

Excellent examples of work on real-time and label-free biosensing applications of structurally engineered porous AAOs have been recently reported by Kumeria and coworkers [183, 184]. They fabricated porous AAO rugate filters (AAO-RFs) by anodizing aluminum in 0.3 M $\text{H}_2\text{C}_2\text{O}_4$ under different pseudosinusoidal potentiostatic conditions controlled by total amount of charge (Q). AAO-RFs were combined with reflection spectroscopy (RfS) in order to develop a biosensing system. The biosensor systems were evaluated and optimized not only by measuring shifts of the characteristic reflection peak with the effective refractive index change, which was achieved by detecting different levels of analytes, but also by performing theoretical modeling based on the Looyenga-Landau-Lifshitz model. For D-glucose sensing, the AAO-RFs biosensing system showed a large linear range from 0.01 to 1.00 M, a low detection limit of 0.01 M, a sensitivity of 4.93 nm M^{-1} , and a linearity of 0.998 [183]. For ionic mercury sensing, it showed a linear



◀ **Fig. 4.24** **a, b** Applied voltage profiles (*red trace*) and measured current transients (*green trace*) for the AAO samples with **a** $Q_o = 0$ C and $Q_o = 4$ C., where Q_o is the charge during the interval of constant potential at 50 V. **c, d** Cross-section SEM images of the respective resulting samples, respectively. The label 2 indicates conical shape of the pores. The label 3 indicates the interface between two cycles. **e–h** Transmittance spectra of the AAO-based DBRs for different Q_o and pore-widening times: **e** $Q_o = 0$ C, **f** $Q_o = 0.5$ C, **g** $Q_o = 1$ C, and **h** $Q_o = 4$ C. The label 1 indicates the beginning of two branchings. Adapted with permission from [182]. Copyright 2013 The American Chemical Society

working range from 1 to 100 μM of Hg^{2+} , low detection limit of 1 μM , and sensitivity of $0.072 \text{ nm } \mu\text{M}^{-1}$, good chemical selectivity over different metal ions (e.g., Co^{2+} , Mg^{2+} , Ni^{2+} , Cu^{2+} , Pb^{2+} , Fe^{3+} , Ca^{2+} , Cr^{6+} , and Ag^+) [184].

4.5 Concluding Remarks

The anodization of aluminum and the resulting self-ordered porous anodic aluminum oxide (AAO) are currently the subject of intensive research in nanotechnology. In this chapter, the most recent advances in structural engineering of porous AAO and applications of porous AAO with tailor-made internal pore geometries have been reviewed. The structure of porous AAO can be characterized by hexagonal arrays of mutually parallel cylindrical pores. Anodization of aluminum under self-ordering regimes yields self-ordered porous AAO, whose pore depth, size, spacing, and density can be conveniently tuned by properly controlling anodizing conditions (i.e., anodizing time, electrolyte, and potential). The porous AAO possesses many useful properties, including excellent thermal stability, chemical inertness, bio-compatibility, and mechanical hardness. In addition, the surface chemistry of pore wall oxide can be conveniently engineered through various methods, including self-assembly, layer-by-layer (LbL) deposition, atomic layer deposition (ALD), chemical-vapor deposition (CVD), sol-gel deposition, and electro/electroless deposition of metals. Over the last two decades, these features have been intensively exploited for the templated syntheses of a variety of low-dimensional functional nanostructures, and also for the development of AAO-based advanced devices, which are difficult or impossible to be fabricated by existing synthetic methods or state-of-the-art lithographic techniques.

Various methods to design and engineer the pore structure of AAO have been developed. These include micromachining of porous AAO, anodization of pre-textured aluminum, multistep anodization with controlled wet-chemical oxide etching after each anodizing step, programmed potential reduction, pulse anodization (PA), and cyclic anodization (CA). These approaches have allowed the researchers to fabricate porous AAOs with a variety of structures, such as porous AAOs with high-aspect-ratio microstructures, sharp featured non-circular pores, non-hexagonal arrangement of pores, symmetrically or asymmetrically modulated pores, funnel-like pores, hierarchical three-dimensional architectures, etc.

Structurally engineered porous AAOs have provided a new degree of freedom in AAO-based syntheses of functional nanostructures. In addition, they have been utilized as platforms for investigating the adsorption and separation behaviors of diverse particles, ions, or biologically important molecules. Recent studies have shown that the structural engineering of porous AAO can result in the generation of optically active structures by imparting tailored optical properties, such as selective transmission, reflection, enhancement, confinement, or guide of light. The demonstrated optically active structures include AAO-based photonic crystals, distributed Bragg reflectors, waveguides, rugate filters, etc. Structurally engineered porous AAOs with custom-designed optical properties have been successfully utilized as platforms for developing various label-free, real-time optical sensing systems for chemical, biological, industrial and environmental analyses. Optical detections of analytes in these sensor systems are based on the change of the effective refractive index of porous AAOs. Analyte detections are not limited to optical method, but can be based on various electrochemical techniques. Apart from precise structural engineering, high selectivity and specificity towards target analytes can be achieved by deliberately engineering the surface chemistry of porous AAOs. As discussed, micromachined porous AAOs can be used as excellent platforms for MEMS devices. Therefore, continuous developments in engineering of structures and surface properties of porous AAOs may lead to a variety of smart and rugged AAO-based sensing devices with multi-performances in near future.

Many electrochemical aspects of aluminum anodization have been disclosed, especially during the past few years. However, the mechanism responsible for the self-organized formation of pores during anodization is still far from being understood and requires further extensive studies. Investigations to this direction are significant, because they may provide viable information in exploring new design rules for noble porous architectures, which are not accessible with the currently available anodization techniques. Future development of innovative anodization techniques, combined with various surface functionalization strategies, will further expand the application field of porous AAOs.

Acknowledgments The financial support from the Hankuk University of Foreign Studies Research Fund of 20151176001 is greatly acknowledged.

References

1. J.W. Diggle, T.C. Downie, C.W. Goulding, Anodic oxide films on aluminum. *Chem. Rev.* **69**, 365–405 (1969)
2. P.G. Sheasby, R. Pinner, *The Surface Treatment and Finishing of Aluminum and Its Alloys*, 6th edn. (Finishing Publications Ltd. & ASM International: Materials Park, Ohio, USA & Stevenage, UK, 2001)
3. H. Masuda, K. Fukuda, Ordered metal nanohole arrays made by a two-step replication of honeycomb structures of anodic alumina. *Science* **268**, 1466–1468 (1995)

4. W. Lee, S.J. Park, Porous anodic aluminum oxide: anodization and templated synthesis of functional nanostructures. *Chem. Rev.* **114**, 7487–7556 (2014)
5. W. Lee, H. Han, A. Lotnyk, M.A. Schubert, S. Senz, M. Alexe, D. Hesse, S. Baik, U. Gösele, Individually addressable epitaxial ferroelectric nanocapacitor arrays with near T_b in⁻² density. *Nat. Nanotechnol.* **3**, 402–407 (2008)
6. C.J. Ingham, J. ter Maat, W.M. de Vos, Where bio meets nano: The many uses for nanoporous aluminum oxide in biotechnology. *Biotechnol. Adv.* **30**, 1089–1099 (2012)
7. S.B. Lee, D.T. Mitchell, L. Trofin, T.K. Nevanen, H. Söderlund, C.R. Martin, Antibody-based bio-nanotube membranes for enantiomeric drug separations. *Science* **296**, 2198–2200 (2002)
8. P. Banerjee, I. Perez, L. Henn-Lecordier, S.B. Lee, G.W. Rubloff, Nanotubular metal-insulator-metal capacitor arrays for energy storage. *Nat. Nanotechnol.* **4**, 292–296 (2009)
9. A.M.M. Jani, D. Losic, N.H. Voelcker, Nanoporous anodic aluminum oxide: advances in surface engineering and emerging applications. *Prog. Mater. Sci.* **58**, 636–704 (2013)
10. A. Santos, T. Kumeria, D. Losic, Nanoporous anodic alumina: a versatile platform for optical biosensors. *Materials* **7**, 4297–4320 (2014)
11. J. Ferré-Borrull, J. Pallarès, G. Macías, L.F. Marsal, Nanostructural engineering of nanoporous anodic alumina for biosensing applications. *Materials* **7**, 5225–5253 (2014)
12. T. Kumeria, A. Santos, D. Losic, Nanoporous anodic alumina platforms: engineered surface chemistry and structure for optical sensing applications. *Sensors* **14**, 11878–11918 (2014)
13. A. Santos, T. Kumeria, D. Losic, Nanoporous anodic aluminum oxide for chemical sensing and biosensors. *TrAC Trends Anal. Chem.* **44**, 25–38 (2013)
14. A. Güntherschulz, H. Betz, Neue Untersuchungen über die elektrolytische Ventilwirkung. *Z. Phys.* **68**, 145–161 (1932)
15. A. Güntherschulz, H. Betz, Die Bewegung der Ionengitter von Isolatoren bei extremen elektrischen Feldstärken. *Z. Phys.* **92**, 367–374 (1934)
16. J.A. Davies, J.P.S. Pringle, R.L. Graham, F. Brown, A radiotracer study of anodic oxidation. *J. Electrochem. Soc.* **109**, 999–1001 (1962)
17. J.A. Davies, B. Domeij, J.P.S. Pringle, F. Brown, The migration of metal and oxygen during anodic film formation. *J. Electrochem. Soc.* **112**, 675–680 (1965)
18. F. Brown, W.D. Mackintosh, The use of Rutherford backscattering to study the behavior of ion-implanted atoms during anodic oxidation of Aluminum: Ar, Kr, Xe, K, Rb, Cs, Cl, Br, and I. *J. Electrochem. Soc.* **120**, 1096–1102 (1973)
19. K. Shimizu, G.E. Thompson, G.C. Wood, Y. Xu, Direct observations of ion-implanted Xenon marker layers in anodic barrier films on aluminum. *Thin Solid Films* **88**, 255–262 (1982)
20. G.E. Thompson, Porous anodic alumina: fabrication, characterization and applications. *Thin Solid Films* **297**, 192–201 (1997)
21. C. Cherki, J. Siejka, Study by nuclear microanalysis and O¹⁸ tracer techniques of the oxygen transport processes and the growth laws for porous anodic oxide layers on aluminum. *J. Electrochem. Soc.* **120**, 784–791 (1973)
22. J. Siejka, C. Ortega, An O¹⁸ study of field-assisted pore formation in compact anodic oxide films on aluminum. *J. Electrochem. Soc.* **124**, 883–891 (1977)
23. P. Skeldon, G.E. Thompson, S.J. Garcia-Vergara, L. Iglesias-Bubianes, C.E. Blanco-Pinzon, A tracer study of porous anodic alumina. *Electrochem. Solid-State Lett.* **9**, B47–B51 (2006)
24. F. Keller, M.S. Hunter, D.L. Robinson, Structural features of oxide coatings on aluminum. *J. Electrochem. Soc.* **100**, 411–419 (1953)
25. M.S. Hunter, P. Fowle, Factors affecting the formation of anodic oxide coatings. *J. Electrochem. Soc.* **101**, 514–519 (1954)
26. T.P. Hoar, J. Yahalom, The initiation of pores in anodic oxide films formed on aluminum in acid solutions. *J. Electrochem. Soc.* **110**, 614–621 (1963)
27. F. Li, L. Zhang, R.M. Metzger, On the growth of highly ordered pores in anodized aluminum oxide. *Chem. Mater.* **10**, 2470–2480 (1998)

28. R.B. Mason, Factors affecting the formation of anodic oxide coatings in sulfuric acid electrolytes. *J. Electrochem. Soc.* **102**, 671–675 (1955)
29. T.P. Hoar, N.F. Mott, A mechanism for the formation of porous anodic oxide films on aluminum. *J. Phys. Chem. Solids* **9**, 97–99 (1959)
30. J.P. O'Sullivan, G.C. Wood, The morphology and mechanism of formation of porous anodic films on aluminum. *Proc. R. Soc. London, Ser. A* **317**, 511–543 (1970)
31. V.P. Parkhutik, V.I. Shershulsky, Theoretical modelling of porous oxide growth on aluminum. *J. Phys. D Appl. Phys.* **25**, 1258–1263 (1992)
32. S.K. Thamida, H.-C. Chang, Nanoscale pore formation dynamics during aluminum anodization. *Chaos* **12**, 240–251 (2002)
33. G.K. Singh, A.A. Golovin, I.S. Aranson, Formation of self-organized nanoscale porous structures in anodic aluminum oxide. *Phys. Rev. B* **73**, 205422 (2006)
34. J. Oh, C.V. Thompson, The role of electric field in pore formation during aluminum anodization. *Electrochim. Acta* **56**, 4044–4051 (2011)
35. A. Baron-Wiecheć, M.G. Burke, T. Hashimoto, H. Liu, P. Skeldon, G.E. Thompson, H. Habazaki, J.-J. Ganem, I.C. Vickridge, Tracer study of pore initiation in anodic alumina formed in phosphoric acid. *Electrochim. Acta* **113**, 302–312 (2013)
36. K.R. Hebert, S.P. Albu, I. Paramasivam, P. Schmuki, Morphological instability leading to formation of porous anodic oxide films. *Nat. Mater.* **11**, 162–166 (2012)
37. S.J. Garcia-Vergara, P. Skeldon, G.E. Thompson, H. Habazaki, A flow model of porous anodic film growth on aluminum. *Electrochim. Acta* **52**, 681–687 (2006)
38. S.J. Garcia-Vergara, D.L. Clere, T. Hashimoto, H. Habazaki, P. Skeldon, G.E. Thompson, Optimized observation of tungsten tracers for investigation of formation of porous anodic alumina. *Electrochim. Acta* **54**, 6403–6411 (2009)
39. S.J. Garcia-Vergara, P. Skeldon, G.E. Thompson, H. Habazaki, Tracer studies of anodic films formed on aluminum in malonic and oxalic acids. *Appl. Surf. Sci.* **254**, 1534–1542 (2007)
40. S.J. Garcia-Vergara, P. Skeldon, G.E. Thompson, H. Habazaki, A tracer investigation of chromic acid anodizing of aluminium. *Surf. Interface Anal.* **39**, 860–864 (2007)
41. J.E. Houser, K.R. Hebert, Stress-driven transport in ordered porous anodic films. *Phys. Status Solidi A* **205**, 2396–2399 (2008)
42. J.E. Houser, K.R. Hebert, Modeling the potential distribution in porous anodic alumina films during steady-state growth. *J. Electrochem. Soc.* **153**, B566–B573 (2006)
43. J.E. Houser, K.R. Hebert, The role of viscous flow of oxide in the growth of self-ordered porous anodic alumina films. *Nat. Mater.* **8**, 415–420 (2009)
44. H. Masuda, M. Satoh, Fabrication of gold nanodot array using anodic porous alumina as an evaporation mask. *Jpn. J. Appl. Phys.* **35**, L126–L129 (1996)
45. H. Masuda, E. Hasegawa, S. Ono, Self-ordering of cell arrangement of anodic porous alumina formed in sulfuric acid solution. *J. Electrochem. Soc.* **144**, L127–L130 (1997)
46. A.P. Li, F. Müller, A. Birner, K. Nielsch, U. Gösele, Hexagonal pore arrays with a 50–420 nm interpore distance formed by self-organization in anodic alumina. *J. Appl. Phys.* **84**, 6023–6026 (1998)
47. O. Nishinaga, T. Kikuchi, S. Natsui, R.O. Suzuki, Rapid fabrication of self-ordered porous alumina with 10-/sub-10-nm-scale nanostructures by selenic acid anodizing. *Sci. Rep.* **3**, 2748 (2013). [10.1038/srep02748](https://doi.org/10.1038/srep02748)
48. H. Masuda, K. Yada, A. Osaka, Self-ordering of cell configuration of anodic porous alumina with large-size pores in phosphoric acid solution. *Jpn. J. Appl. Phys.* **37**, L1340–L1342 (1998)
49. K. Nielsch, J. Choy, K. Schwirn, R.B. Wehrspohn, U. Gösele, Self-ordering regimes of porous alumina: the 10% porosity rule. *Nano Lett.* **2**, 677–680 (2002)
50. S. Shingubara, K. Morimoto, H. Sakaue, T. Takahagi, Self-organization of a porous alumina nanohole array using a sulfuric/oxalic acid mixture as electrolyte. *Electrochem. Solid-State Lett.* **7**, E15–E17 (2004)
51. C. Sun, J. Luo, L. Wu, J. Zhang, Self-ordered anodic alumina with continuously tunable pore intervals from 410 to 530 nm. *ACS Appl. Mater. Interfaces* **2**, 1299–1302 (2010)

52. J.M. Kape, The use of malonic acid as an anodising electrolyte. *Metallurgia* **60**, 181–191 (1959)
53. J.M. Kape, Unusual anodizing processes and their practical significance. *Electroplat. Metal Finish.* **14**, 407–415 (1961)
54. J.M. Kape, Anodizing in aqueous solutions of organic carboxylic acids. *Trans. Inst. Met. Finish.* **45**, 34–42 (1967)
55. S. Ono, M. Saito, M. Ishiguro, H. Asoh, Controlling factor of self-ordering of anodic porous alumina. *J. Electrochem. Soc.* **151**, B473–B478 (2004)
56. S. Ono, M. Saito, H. Asoh, Self-ordering of anodic porous alumina formed in organic acid electrolytes. *Electrochim. Acta* **51**, 827–833 (2005)
57. T. Kikuch, O. Nishinaga, S. Natsui, R.O. Suzuki, Self-ordering behavior of anodic porous alumina via selenic acid anodizing. *Electrochim. Acta* **137**, 728–735 (2014)
58. I. Vrublevsky, V. Parkoun, J. Schreckenbach, G. Marx, Study of porous oxide film growth on aluminum in oxalic acid using a re-anodizing technique. *Appl. Surf. Sci.* **227**, 282–292 (2004)
59. G.D. Sulka, K.G. Parkola, Temperature influence on well-ordered nanopore structures grown by anodizing of aluminum in sulphuric acid. *Electrochim. Acta* **52**, 1880–1888 (2007)
60. W. Chen, J.-S. Wu, X.-H. Xia, Porous anodic alumina with continuously manipulated pore/cell size. *ACS Nano* **2**, 959–965 (2008)
61. J. Martín, C.V. Manzano, O. Caballero-Calero, M. Martín-González, High-aspect-ratio and highly ordered 15-nm porous alumina templates. *ACS Appl. Mater. Interf.* **5**, 72–79 (2013)
62. S. Ikonopisov, A. Girginov, M. Machkova, Post-breakdown anodization of aluminum. *Electrochim. Acta* **22**, 1283–1286 (1977)
63. J.M. Albella, I. Montero, J.M. Martínez-Duart, Electron injection and avalanche during the anodic oxidation of tantalum. *J. Electrochem. Soc.* **131**, 1101–1104 (1984)
64. S.Z. Chu, K. Wada, S. Inoue, M. Isogai, Y. Katsuta, A. Yasumori, Large-scale fabrication of ordered nanoporous alumina films with arbitrary pore intervals by critical-potential anodization. *J. Electrochem. Soc.* **153**, B384–B391 (2006)
65. S. Ono, M. Saito, H. Asoh, Self-ordering of anodic porous alumina induced by local current concentration: Burning. *Electrochem. Solid-Sate Lett.* **7**, B21–B24 (2004)
66. G.C. Tu, I.T. Chen, K. Shimizu, The temperature rise and burning for high rate anodizing of aluminum in oxalic acid. *J. Jpn. Inst. Light Met.* **40**, 382–389 (1990)
67. P. Csokán, Beiträge zur Kenntnis der anodischen Oxydation von Aluminium verdünnter, kalter Schwefelsäure. *Metalloberfläche* **15**, B49–B53 (1961)
68. V.P. Csokán, M. Holló, Beitrag zur Frage des Bildungsmechanismus von anodisch erzeugten Hartoxydschichten. *Werkst. Korros.* **12**, 288–295 (1961)
69. P. Csokán, C.C. Sc., Hard anodizing. *Electroplat. Metal Finishing* **15**, 75–82 (1962)
70. P. Csokán, Some observations on the growth mechanism of hard anodic oxide coatings on aluminium. *Trans. Inst. Met. Finish.* **41**, 51–56 (1964)
71. S. John, V. Balasubramanian, B.A. Shenoi, Hard anodizing aluminium and its alloys—AC in sulphuric acid—sodium sulphate bath. *Met. Finish.* **82**, 33–39 (1984)
72. B. Olbertz, Hartanodisieren eröffnet aluminium vielfältige technische Anwendungsmöglichkeiten. *Aluminium* **3**, 268–270 (1988)
73. J.G. Hecker, Aluminum hard coats. *Prod. Finish.* **53**, 88–92 (1988)
74. A. Rajendra, B.J. Parmar, A.K. Sharma, H. Bhojraj, M.M. Nayak, K. Rajanna, Hard anodisation of aluminium and its application to sensorics. *Surf. Eng.* **21**, 193–197 (2005)
75. S.-Z. Chu, K. Wada, S. Inoue, M. Isogai, A. Yasumori, Fabrication of ideally ordered nanoporous alumina films and integrated alumina nanotubue arrays by high-field anodization. *Adv. Mater.* **17**, 2115–2119 (2005)
76. K. Schwirn, *Harte anodisation von aluminium mit Verdünnter Schwefeläure* (Martin-Luther-Universität Halle-Wittenberg, Halle (Saale), 2008)
77. K. Schwirn, W. Lee, R. Hillebrand, M. Steinhart, K. Nielsch, U. Gösele, Self-ordered anodic aluminum oxide formed by H₂SO₄ hard anodization. *ACS Nano* **2**, 302–310 (2008)

78. W. Lee, R. Ji, U. Gösele, K. Nielsch, Fast fabrication of long-range ordered porous alumina membranes by hard anodization. *Nat. Mater.* **5**, 741–747 (2006)
79. W. Lee, K. Nielsch, U. Gösele, Self-ordering behavior of nanoporous anodic aluminum oxide (AAO) in malonic acid anodization. *Nanotechnology* **18**, 475713 (2007)
80. Y. Li, M. Zheng, L. Ma, W. Shen, Fabrication of highly ordered nanoporous alumina films by stable high-field anodization. *Nanotechnology* **17**, 5101–5105 (2006)
81. Y.B. Li, M.J. Zheng, L. Ma, High-speed growth and photoluminescence of porous anodic alumina films with controllable interpore distances over a large range. *Appl. Phys. Lett.* **91**, 073109 (2007)
82. M.A. Kashi, A. Ramazani, M. Noormohammadi, M. Zarei, P. Marashi, Optimum self-ordered nanopore arrays with 130–270 nm interpore distances formed by hard anodization in sulfuric/oxalic acid mixtures. *J. Phys. D Appl. Phys.* **40**, 7032–7040 (2007)
83. Y. Li, Z.Y. Ling, S.S. Chen, J.C. Wang, Fabrication of novel porous anodic alumina membranes by two-step hard anodization. *Nanotechnology* **19**, 225604 (2008)
84. M.S. Hunter, P. Fowle, Determination of barrier layer thickness of anodic oxide coatings. *J. Electrochem. Soc.* **101**, 481–485 (1954)
85. W. Lee, J.-C. Kim, U. Gösele, Spontaneous current oscillations during hard anodization of aluminum under potentiostatic conditions. *Adv. Funct. Mater.* **20**, 21–27 (2010)
86. S.-S. Tan, M.L. Reed, H. Han, R. Boudreau, High aspect ratio microstructures on porous anodic aluminum oxide. *Proceedings of the 8th International Workshop on Microelectro Mechanical System (MEMS-95)*, Amsterdam, 1995; pp. 267–272
87. A.-P. Li, F. Müller, A. Birner, K. Nielsch, U. Gösele, Fabrication and microstructuring of hexagonally ordered two-dimensional nanopore arrays in anodic alumina. *Adv. Mater.* **11**, 483–487 (1999)
88. D. Routkevitch, A.N. Govyadinov, P.P. Mardilovich, High aspect ratio, high resolution ceramic MEMS. *Proceedings of ASME International Mechanical Engineering*, vol. 2, ASME Orlando, FL, 2000, pp. 39–44
89. D. Routkevitch, O. Polyakov, D. Deininger, C. Kostecky, Nanostructured gas microsensor platform. In *NSTI Nanotech*, Anaheim **2**, 266–268 (2005)
90. H. Masuda, H. Yamada, M. Satoh, H. Asoh, M. Nakao, T. Tamamura, Highly ordered nanochannel-array architecture in anodic alumina. *Appl. Phys. Lett.* **71**, 2770–2772 (1997)
91. H. Masuda, H. Asoh, M. Watanabe, K. Nishio, M. Nakao, T. Tamamura, Square and triangular nanohole array architectures in anodic alumina. *Adv. Mater.* **13**, 189–192 (2001)
92. I. Mikulskas, S. Juodkakis, R. Tomašiūnas, J.G. Dumas, Aluminum oxide photonic crystals grown by a new hybrid method. *Adv. Mater.* **13**, 1574–1577 (2001)
93. J. Choi, K. Nielsch, M. Reiche, R.B. Wehrspohn, U. Gösele, Fabrication of monodomain alumina pore arrays with an interpore distance smaller than the lattice constant of the imprint stamp. *J. Vac. Sci. Technol., B* **21**, 763–766 (2003)
94. W. Lee, R. Ji, C.A. Ross, U. Gösele, K. Nielsch, Wafer-scale Ni imprint stamps for porous alumina membranes based on interference lithography. *Small* **2**, 978–982 (2006)
95. S. Fournier-Bidoz, V. Kitaev, D. Routkevitch, I. Manners, G.A. Ozin, Highly ordered nanosphere imprinted nanochannel alumina (NINA). *Adv. Mater.* **16**, 2193–2196 (2004)
96. H. Masuda, Y. Matsui, M. Yotsuya, F. Matsumoto, K. Nishio, Fabrication of highly ordered anodic porous alumina using self-organized polystyrene particle array. *Chem. Lett.* **33**, 584–585 (2004)
97. C.Y. Liu, A. Datta, Y.L. Wang, Ordered anodic alumina nanochannels on focused-ion-beam-prepatterned aluminum surfaces. *Appl. Phys. Lett.* **78**, 120–122 (2001)
98. B. Chen, K. Lu, Z. Tian, Gradient and alternating diameter nanopore templates by focused ion beam guided anodization. *Electrochim. Acta* **56**, 435–440 (2010)
99. B. Chen, K. Lu, Z. Tian, Novel patterns by focused ion beam guided anodization. *Langmuir* **27**, 800–808 (2011)
100. R. Krishnan, C.V. Thompson, Monodomain high-aspect-ratio 2D and 3D ordered porous alumina structures with independently controlled pore spacing and diameter. *Adv. Mater.* **18**, 988–992 (2007)

101. Z. Sun, H.K. Kim, Growth of ordered, single-domain, alumina nanopore arrays with holographically patterned aluminum films. *Appl. Phys. Lett.* **81**, 3458–3460 (2010)
102. B. Kim, S. Park, T.J. McCarthy, T.P. Russell, Fabrication of ordered anodic aluminum oxide using a solvent-induced array of block-copolymer micelles. *Small* **3**, 1869–1872 (2007)
103. T.S. Kustandi, W.W. Loh, H. Gao, H.Y. Low, Wafer-scale near-perfect ordered porous alumina on substrates by step and flash imprint lithography. *ACS Nano* **4**, 2561–2568 (2010)
104. K.-L. Lai, M.-H. Hon, I.-C. Leu, Fabrication of ordered nanoporous anodic alumina prepatterned by mold-assisted chemical etching. *Nanoscale Res. Lett.* **6**, 157 (2011)
105. H. Masuda, M. Yotsuya, M. Asano, K. Nishio, M. Nakao, A. Yokoo, T. Tamamura, Self-repair of ordered pattern of nanometer dimensions based on self-compensation properties of anodic porous alumina. *Appl. Phys. Lett.* **78**, 826–828 (2001)
106. J.T. Smith, Q. Huang, A.D. Franklin, D.B. Janes, T.D. Sands, Highly ordered diamond and hybrid triangle-diamond patterns in porous anodic alumina thin films. *Appl. Phys. Lett.* **93**, 043108 (2008)
107. G.E. Thompson, Y. Xu, P. Skeldon, K. Shimizu, S.H. Han, G.C. Wood, Anodic oxidation of aluminum. *Philos. Mag. B* **55**, 651–667 (1987)
108. G.E. Thompson, R.C. Furneaux, G.C. Wood, Electron microscopy of ion beam thinned porous anodic films formed on aluminium. *Corros. Sci.* **18**, 481–498 (1978)
109. I. Vrublevsky, V. Parkoun, V. Sokol, J. Schreckenbach, Analysis of chemical dissolution of the barrier layer of porous oxide on aluminum thin films using a re-anodizing technique. *Appl. Surf. Sci.* **252**, 227–233 (2005)
110. S. Ono, H. Ichinose, N. Masuko, The high resolution observation of porous anodic films formed on aluminum in phosphoric acid solution. *Corros. Sci.* **33**, 841–850 (1992)
111. G.C. Wood, P. Skeldon, G.E. Thompson, K. Shimizu, A model for the incorporation of electrolyte species into anodic alumina. *J. Electrochem. Soc.* **143**, 74–83 (1996)
112. H. Han, S.-J. Park, J.S. Jang, H. Ryu, K.J. Kim, S. Baik, W. Lee, In-situ determination of the pore opening point during wet-chemical etching of the barrier layer of porous anodic aluminum oxide (AAO): non-uniform impurity distribution in anodic oxide. *ACS Appl. Mater. Interfaces* **5**, 3441–3448 (2013)
113. Y. Yamamoto, N. Baba, S. Tajima, Coloured materials and photoluminescence centres in anodic film on aluminium. *Nature* **289**, 572–584 (1981)
114. W.L. Xu, M.J. Zheng, S. Wu, W.Z. Sheng, Effects of high-temperature annealing on structural and optical properties of highly ordered porous alumina membranes. *Appl. Phys. Lett.* **85**, 4364–4366 (2004)
115. Y. Du, W.L. Cai, C.M. Mo, J. Chen, L.D. Zhang, X.G. Zhu, Preparation and photoluminescence of alumina membranes with ordered pore arrays. *Appl. Phys. Lett.* **74**, 2951–2953 (1999)
116. G.H. Li, Y. Zhang, Y.C. Wu, L.D. Zhang, Wavelength dependent photoluminescence of anodic alumina membranes. *J. Phys.: Condens. Matter* **15**, 8663–8671 (2003)
117. A. Santos, M. Alba, M.M. Rahman, P. Formentin, J. Ferré-Borrull, J. Pallarès, L.F. Marsal, Structural tuning of photoluminescence in nanoporous anodic alumina by hard anodization in oxalic and malonic acids. *Nanoscale Res. Lett.* **7**, 228 (2012)
118. S. Ono, N. Masuko, The duplex structure of cell walls of porous anodic films formed on aluminum. *Corros. Sci.* **33**, 503–507 (1992)
119. G.E. Thompson, R.C. Furneaux, G.C. Wood, STEM/EDAS analysis of the cell walls in porous anodic films formed on aluminum. *J. Electrochem. Soc.* **125**, 1480–1482 (1978)
120. M.C. Thornton, R.C. Furneaux, Transmission electron microscopy and digital X-ray mapping of ion-beam-thinned porous anodic films formed on aluminium. *J. Mater. Sci. Lett.* **10**, 622–624 (1991)
121. K. Huang, L. Pu, Y. Shi, P. Han, R. Zhang, Y.D. Zheng, Photoluminescence oscillations in porous alumina films. *Appl. Phys. Lett.* **89**, 201118 (2006)
122. D.A.G. Bruggeman, Derechnung verschiedener physikalischer Konstanten von heterogenen Substanzen: I. Dielektrizitätskonstanten und Leitfähigkeiten der Mischkörper aus isotropen Substanzen. *Ann. Phys.* **24**, 636–664 (1935)

123. A. Santos, V.S. Balderrama, M. Alba, P. Formentín, J. Ferré-Borrull, J. Pallarès, L.F. Marsal, Nanoporous anodic alumina barcodes: toward smart optical biosensors. *Adv. Mater.* **24**, 1050–1054 (2012)
124. A. Santos, T. Kumeria, D. Losic, Optically optimized photoluminescent and interferometric biosensors based on nanoporous anodic alumina: a comparison. *Anal. Chem.* **85**, 7904–7911 (2013)
125. F. Casanova, C.E. Chiang, C.-P. Li, I.V. Roshchin, A.M. Ruminski, M.J. Sailor, I.K. Schuller, Effect of surface interactions on the hysteresis of capillary condensation in nanopores. *Europhys. Lett.* **81**, 26003 (2008)
126. F. Casanova, C.E. Chiang, C.-P. Li, I.V. Roshchin, A.M. Ruminski, M.J. Sailor, I.K. Schuller, Gas adsorption and capillary condensation in nanoporous alumina films. *Nanotechnology* **19**, 315709 (2008)
127. S.D. Alvarez, C.-P. Li, C.E. Chiang, I.K. Schuller, M.J. Sailor, A label-free porous alumina interferometric immunosensor. *ACS Nano* **3**, 3301–3307 (2009)
128. T. Kumeria, D. Losic, Reflective interferometric gas sensing using nanoporous anodic aluminium oxide (AAO). *Phys. Status Solidi RRL* **5**, 406–408 (2011)
129. T. Kumeria, L. Parkinson, D. Losic, A nanoporous interferometric micro-sensor for biomedical detection of volatile sulphur compounds. *Nanoscale Res. Lett.* **6**, 634 (2011)
130. T. Kumeria, D. Losic, Controlling interferometric properties of nanoporous anodic aluminum oxide. *Nanoscale Res. Lett.* **7**, 88 (2012)
131. T. Kumeria, A. Santos, D. Losic, Ultrasensitive nanoporous interferometric sensor for label-free detection of gold(III) ions. *ACS Appl. Mater. Interfaces* **5**, 11783–11790 (2013)
132. B. He, S.J. Son, S.B. Lee, Shape-coded silica nanotubes for biosensing. *Langmuir* **22**, 8263–8265 (2006)
133. A. Santos, P. Formentín, J. Pallarès, J. Ferré-Borrull, L.F. Marsal, Structural engineering of nanoporous anodic alumina funnels with high aspect ratio. *J. Electroanal. Chem.* **655**, 73–78 (2011)
134. B. He, S.J. Son, S.B. Lee, Suspension array with shape-coded silica nanotubes for multiplexed immunoassays. *Anal. Chem.* **79**, 5257–5263 (2007)
135. J. Li, C. Li, C. Chen, Q. Hao, Z. Wang, J. Zhu, X. Gao, Facile method for modulating the profiles and periods of self-ordered three-dimensional alumina taper-nanopores. *ACS Appl. Mater. Interfaces* **4**, 5678–5683 (2012)
136. A. Santos, T. Kumeria, Y. Wang, D. Losic, In situ monitored engineering of inverted nanoporous anodic alumina funnels: on the precise generation of 3D optical nanostructures. *Nanoscale* **6**, 9991–9999 (2014)
137. T. Nagaura, F. Takeuchi, Y. Yamauchi, K. Wada, S. Inoue, Fabrication of ordered Ni nanocones using a porous anodic alumina template. *Electrochem. Commun.* **10**, 681–685 (2008)
138. T. Nagaura, F. Takeuchi, S. Inoue, Fabrication and structural control of anodic alumina films with inverted cone porous structure using multi-step anodizing. *Electrochim. Acta* **53**, 2109–2114 (2008)
139. T. Yanagishita, T. Kondo, K. Nishio, H. Masuda, Optimization of antireflection structures of polymer based on nanoimprinting using anodic porous alumina. *J. Vac. Sci. Technol., B* **26**, 1856–1859 (2008)
140. G. Macías, L.P. Hernández-Eguía, J. Ferré-Borrull, J. Pallarès, L.F. Marsal, Gold-coated ordered nanoporous anodic alumina bilayers for future label-free interferometric biosensors. *ACS Appl. Mater. Interfaces* **5**, 8093–8098 (2013)
141. H. Takahashi, M. Nagayama, H. Akahori, A. Kitahara, Electron-microscopy of porous anodic oxide films on aluminium by ultra-thin sectioning technique. Part 1. The structural change of the film during the current recovery period. *J. Electron Microscopy* **22**, 149–157 (1973)
142. J.W. Diggle, T.C. Downie, C.W. Goulding, Processes involved in reattainment of steady-state conditions for the anodizing of aluminium following formation voltage changes. *J. Electrochem. Soc.* **116**, 737–740 (1969)

143. W. Lee, J.-C. Kim, Highly ordered porous alumina with tailor-made pore structures fabricated by pulse anodization. *Nanotechnology* **21**, 485304 (2010)
144. W. Lee, K. Schwirn, M. Steinhart, E. Pippel, R. Scholz, U. Gösele, Structural engineering of nanoporous anodic aluminum oxide by pulse anodization of aluminum. *Nat. Nanotechnol.* **3**, 234–239 (2008)
145. R.C. Furneaux, W.R. Rigby, A.P. Davidson, The formation of controlled porosity membranes from anodically oxidized aluminium. *Nature* **337**, 147–149 (1989)
146. J.M. Montero-Moreno, M. Belenguer, M. Sarret, C.M. Müller, Production of alumina templates suitable for electrodeposition of nanostructures using stepped techniques. *Electrochim. Acta* **54**, 2529–2535 (2009)
147. K. Nielsch, F. Müller, A.-P. Li, U. Gösele, Uniform nickel deposition into ordered alumina pores by pulsed electrodeposition. *Adv. Mater.* **12**, 582–586 (2000)
148. G. Sauer, G. Brehm, S. Chneider, K. Nielsch, R.B. Wehrspohn, J. Choi, H. Hofmeister, U. Gösele, Highly ordered monocrystalline silver nanowire arrays. *J. Appl. Phys.* **91**, 3243–3247 (2002)
149. W. Cheng, M. Steinhart, U. Gösele, R.B. Wehrspohn, Tree-like alumina nanopores generated in a non-steady-state anodization. *J. Mater. Chem.* **17**, 3493–3495 (2007)
150. J. Choi, G. Sauer, K. Nielsch, R.B. Wehrspohn, U. Gösele, Hexagonally arranged monodisperse silver nanowires with adjustable diameter and high aspect ratio. *Chem. Mater.* **15**, 776–779 (2003)
151. W. Lee, R. Scholz, K. Nielsch, U. Gösele, A template-based electrochemical method for the synthesis of multisegmented metallic nanotubes. *Angew. Chem. Int. Ed.* **44**, 6050–6054 (2005)
152. G. Jeon, M. Jee, S.Y. Yang, B.-Y. Lee, S.K. Jang, J.K. Kim, Hierarchically self-organized monolithic nanoporous membrane for excellent virus enrichment. *ACS Appl. Mater. Interfaces* **6**, 1200–1206 (2014)
153. J. Li, C. Papadopoulos, J. Xu, Growing Y-junction carbon nanotubes. *Nature* **402**, 253–254 (1999)
154. C. Papadopoulos, A. Rakitin, J. Li, A.S. Vedenev, J.M. Xu, Electronic transport in Y-junction carbon nanotubes. *Phys. Rev. Lett.* **85**, 3476–3479 (2000)
155. Y.C. Sui, J.A. González-León, A. Bermúdez, J.M. Saniger, Synthesis of multi branched carbon nanotubes in porous anodic aluminum oxide template. *Carbon* **39**, 1709–1715 (2001)
156. T. Gao, G. Meng, J. Zhang, S. Sun, L. Zhang, Template synthesis of Y-junction metal nanowires. *Appl. Phys. A* **74**, 403–406 (2002)
157. G. Meng, Y.J. Jung, A. Cao, R. Vajtai, P.M. Ajayan, Controlled fabrication of hierarchically branched nanopores, nanotubes, and nanowires. *Proc. Natl. Acad. Sci. U.S.A.* **102**, 7074–7078 (2005)
158. C. Shuoshuo, L. Zhiyuan, H. Xing, L. Yi, Controlled growth of branched channels by a factor of $1/\sqrt{n}$ anodizing voltage? *J. Mater. Chem.* **19**, 5717–5719 (2009)
159. A.Y.Y. Ho, H. Gao, Y.C. Lam, I. Rodríguez, Controlled fabrication of multitiered three-dimensional nanostructures in porous alumina. *Adv. Funct. Mater.* **18**, 2057–2063 (2008)
160. K. Pitzschel, J.M.M. Moreno, J. Escrig, O. Albrecht, K. Nielsch, J. Bachmann, Controlled introduction of diameter modulations in arrayed magnetic iron oxide nanotubes. *ACS Nano* **3**, 3463–3469 (2009)
161. D.J. Arrowsmith, A.W. Clifford, D.A. Moth, Fracture of anodic oxide formed on aluminum in sulphuric acid. *J. Mater. Sci. Lett.* **5**, 921–922 (1986)
162. K. Wada, T. Shimohira, M. Amada, N. Baba, Microstructure of porous anodic oxide films on aluminium. *J. Mater. Sci.* **21**, 3810–3816 (1986)
163. W. Lee, R. Scholz, U. Gösele, A continuous process for structural well-defined Al_2O_3 nanotubes based on pulse anodization of aluminum. *Nano Lett.* **8**, 2155–2160 (2008)
164. K.E. La Flamme, G. Mor, D. Gong, T. La Tempa, V.A. Fusaro, C.A. Grimes, T.A. Desai, Nanoporous alumina capsules for cellular macroencapsulation: transport and biocompatibility. *Diabetes Technol. Ther.* **7**, 684–694 (2005)

165. E.E.L. Swan, K.C. Papat, C.A. Grimes, T.A. Desai, Fabrication and evaluation of nanoporous alumina membranes for osteoblast culture. *J. Biomed. Mater. Res., Part A* **72A**, 288–295 (2005)
166. B. Jongsomjit, J. Panpranot, J.G. Goodwin Jr, Co-support compound formation in alumina-supported cobalt catalysts. *J. Catal.* **204**, 98–109 (2001)
167. E.P. Gusev, M. Copel, E. Cartier, I.J.R. Baumvol, C. Krug, M.A. Gribelyuk, High-resolution depth profiling in ultrathin Al_2O_3 films on Si. *Appl. Phys. Lett.* **76**, 176–178 (2000)
168. Y. Wang, A. Santos, G. Kaur, A. Evdokiou, D.L. Losic Jr, Structurally engineered anodic alumina nanotubes as nano-carriers for delivery of anticancer therapeutics. *Biomaterials* **35**, 5517–5526 (2014)
169. A. Santos, L. Vojkuvka, M. Alba, V.S. Balderrama, J. Ferré-Borrull, J. Pallarès, L.F. Marsal, Understanding and morphology control of pore modulations in nanoporous anodic alumina by discontinuous anodization. *Phys. Status Solidi A* **209**, 2045–2048 (2012)
170. D. Losic, M. Lillo, D. Losic Jr, Porous alumina with shaped pore geometries and complex pore architectures fabricated by cyclic anodization. *Small* **5**, 1392–1397 (2009)
171. D. Losic, D. Losic Jr, Preparation of porous anodic alumina with periodically perforated pores. *Langmuir* **25**, 5426–5431 (2009)
172. E.A. Avrutin, V.B. Gorfinkel, S. Luryi, K.A. Shore, Control of surface-emitting laser diodes by modulating the distributed Bragg mirror reflectivity: small-signal analysis. *Appl. Phys. Lett.* **63**, 2460–2462 (1993)
173. J. Yoon, W. Lee, E.L. Thomas, Optically pumped surface-emitting lasing using self-assembled block-copolymer-distributed Bragg reflectors. *Nano Lett.* **6**, 211–2214 (2006)
174. L. Chen, E. Towe, Nanowire lasers with distributed-Bragg-reflector mirrors. *Appl. Phys. Lett.* **89**, 053125 (2006)
175. B. Wang, G.T. Fei, M. Wang, M.G. Kong, L.D. Zhang, Preparation of photonic crystals made of air pores in anodic alumina. *Nanotechnology* **18**, 365601 (2007)
176. W.J. Zheng, G.T. Fei, B. Wang, Z. Jin, L.D. Zhang, Distributed Bragg reflector made of anodic alumina membrane. *Mater. Lett.* **63**, 706–708 (2009)
177. W.J. Zheng, G.T. Fei, B. Wang, L.D. Zhang, Modulation of transmission spectra of anodized alumina membrane distributed bragg reflector by controlling anodization temperature. *Nanoscale Res. Lett.* **4**, 665–667 (2009)
178. G.L. Shang, G.T. Fei, Y. Zhang, P. Yan, S.H. Xu, L.D. Zhang, Preparation of narrow photonic bandgaps located in the near infrared region and their applications in ethanol gas sensing. *J. Mater. Chem. C* **1**, 5285–5291 (2013)
179. G.L. Shang, G.T. Fei, Y. Zhang, P. Yan, S.H. Xu, H.M. Ouyang, L.D. Zhang, Fano resonance in anodic aluminum oxide based photonic crystals. *Sci. Rep.* **4**, 3601 (2014)
180. G.L. Shang, G.T. Fei, S.H. Xu, P. Yan, L.D. Zhang, Preparation of the very uniform pore diameter of anodic alumina oxidation by voltage compensation mode. *Mater. Lett.* **110**, 156–159 (2013)
181. H. Xing, L. Zhi-Yuan, C. Shuo-Shuo, H. Xin-Hua, Influence of light scattering on transmission spectra of photonic crystals of anodized alumina. *Chin. Phys. Lett.* **25**, 3284–3287 (2008)
182. M.M. Rahman, L.F. Marsal, J. Pallarès, J. Ferré-Borrull, Tuning the photonic stop bands of nanoporous anodic alumina-based distributed bragg reflectors by pore widening. *ACS Appl. Mater. Interfaces* **5**, 13375–13381 (2013)
183. T. Kumeria, M.M. Rahman, A. Santos, J. Ferré-Borrull, L.F. Marsal, D. Losic, Structural and optical nanoengineering of nanoporous anodic alumina rugate filters for real-time and label-free biosensing applications. *Anal. Chem.* **86**, 1837–1844 (2014)
184. T. Kumeria, M.M. Rahman, A. Santos, J. Ferré-Borrull, L.F. Marsal, D. Losic, Nanoporous anodic alumina rugate filters for sensing of ionic mercury: toward environmental point-of analysis systems. *ACS Appl. Mater. Interfaces* **6**, 12971–12978 (2014)